nature communications

Article

https://doi.org/10.1038/s41467-026-73453-x

Measuring multi-site pulse transit time with an AI-enabled mmWave radar

Received: 10 April 2025

Accepted: 8 May 2026

Published online: 25 May 2026

Check for updates

Jiangyifei Zhu[1,4], Kuang Yuan[1,4], Akarsh Prabhakara[2], Yunzhi Li[1], Gongwei Wang[1], Kelly Michaelsen[3], Justin Chan[1] ✉ & Swarun Kumar[1] ✉

Pulse Transit Time (PTT) is a measure of arterial stiffness and a physiological marker associated with cardiovascular function, with an inverse relationship to diastolic blood pressure (DBP). We present an AI-enabled mmWave system for contactless multi-site PTT measurement using a single radar. By leveraging radar beamforming and deep learning algorithms our system simultaneously measures PTT and estimates diastolic blood pressure at multiple sites. The system was evaluated across three physiological pathways – heart-to-radial artery, heart-to-carotid artery, and mastoid area-to-radial artery – achieving correlation coefficients of 0.75–0.86 compared to contact-based reference sensors for measuring PTT. Furthermore, the system demonstrated correlation coefficients of 0.90–0.91 for estimating DBP, and achieved a mean error of -0.62–0.06 mmHg and standard deviation of 4.54–5.20 mmHg, meeting the FDA's AAMI guidelines for non-invasive blood pressure monitors. These results suggest that our proposed system has the potential to provide a non-invasive measure of cardiovascular health across multiple regions of the body.

Frequent monitoring of cardiovascular health can facilitate timely interventions including lifestyle changes such as exercise and diet, as well as pharmacologic changes like antihypertensive drugs[1]. Increased arterial stiffness is associated with a higher risk of cardiovascular conditions including hypertension[2], stroke[3], coronary artery disease[3], sleep apnea[4,5], and Alzheimer's disease[6], and can be quantified using pulse transit time (PTT), the time it takes for a pulse wave to travel between a proximal and distal site within an artery[7]. In addition, pulse transit time is indirectly related to diastolic blood pressure (DBP) and has been explored as the basis for cuff-less blood pressure monitoring[8–12]. The ability to measure PTT contactlessly at multiple sites along the body has the potential to support pre-screening of cardiovascular diseases and long-term tracking of disease progression, particularly for high-risk populations such as older adults and individuals with chronic conditions[13]. This is because PTT varies across different body sites with distal arterial stiffness relating to peripheral disease burden and proximal stiffness relating to central arterial health[14,15], with site-specific differences influenced by underlying physiologic stress mechanisms[16]. This suggests that multi-site PTT measurements can capture relative stiffness between pathways such as a mismatch between central and peripheral stiffness[17,18], and may provide a more comprehensive assessment of cardiovascular hemodynamics than a single measurement[19–22].

Arterial stiffness can be measured using contact-based methods, including pulse tonometry for arterial pressure assessment[23], photoplethysmography (PPG) for detecting light absorption changes[24], inertial measurement units (IMU) for capturing pulse motion[25], and electrodes or wearable sensors[9,26–32], which may cause skin irritation and discomfort. Contactless measurement systems have leveraged cameras[33–37] to measure PPG, and laser-doppler vibrometry[38] to measure the surface displacement at multiple arterial sites. However, such optical-based systems may not work well in low-lighting conditions or when objects like clothing block the device's view. More recently, radar-based approaches have been proposed, leveraging millimeter-wave (mmWave)[39–43], or microwave[44], to measure the seismocardiogram (SCG) at the chest and ballistocardiogram (BCG) at the head.

[1]Department of Electrical and Computer Engineering, Carnegie Mellon University, Pittsburgh, PA, USA. [2]Department of Computer Sciences, University of Wisconsin-Madison, Madison, WI, USA. [3]Department of Anesthesiology & Pain Medicine, University of Washington, Seattle, WA, USA. [4]These authors contributed equally: Jiangyifei Zhu, Kuang Yuan. ✉e-mail: justinchan@cmu.edu; swarun@cmu.edu

However, existing radar-based systems either require multiple sensor units to measure multiple arterial points[39,40], which can be challenging to deploy and precisely position, or are limited to measuring a single PTT pair[42,45,46].

Here, we present *PolyPulse*, a proof-of-concept AI-enabled mmWave radar system that enables simultaneous, contactless measurements of pulse transit time and DBP estimation along three key physiological pathways along the upper body using a single radar. Measuring all sites concurrently enables a synchronized, beats-matched comparison of the same cardiac cycle across multiple physiological pathways, which is important given that PTT exhibits meaningful beat to beat variability[47,48]. In contrast, prior approaches that use one radar per arterial site[39,40] would require sequentially repositioning the radar, yielding measurements from different beats and time windows during which heart rate and waveform morphology can change due to physiologic and environmental factors[49,50]. This can result in measurements that conflate the effects of cardiac cycle variability with true arterial stiffness effects along different pathways. Finally, using a single radar streamlines the workflow by eliminating repeated repositioning and supports convenient upright measurements.

Our system transmits chirp signals toward a seated individual and performs fine-grained beamforming on the reflected signal to capture the subtle bodily movements caused by cardiac activity. The design leverages a neural network model to process the reflection waveforms from the apex of the heart, the mastoid area at the head, the radial artery at the wrist, and the carotid artery at the neck. Using these signals, the model jointly estimates pulse transit times and diastolic blood pressure for physiological pathways that originate from the heart and head and extend to distal points at the wrist or neck. Our wireless radar system is compact and measures 16.5 × 14 cm, which can fit within the form factor of smart home devices. Given the increasing prevalence of mmWave radars on consumer devices, our proposed multi-site PTT system can make remote monitoring of cardiovascular health at home more comprehensive and accessible.

Results

Concept and prototype

As the heart beats, it generates pulse waves that propagate through arterial pathways in the body. This pulsatile flow causes rhythmic expansion and contraction of the arterial walls, which in turn results in minute superficial displacements of the skin (Fig. 1a)[51]. *PolyPulse* transmits FMCW signals from 77 to 81 GHz towards a seated individual and analyzes both the phase and magnitude of the reflected signals at key physiological sites where a cardiac signal can be measured. The phase variations of the reflections correspond to superficial displacement of the skin at distal sites (Fig. 1b, c), while the magnitude variations correspond to changes in signal absorption due to blood flow that occur throughout each cardiac cycle. Our system measures cardiac signals by capturing reflections from two proximal reference points and two distal arterial points. For the proximal reference point, our radar captures reflections from the apex of the heart at the chest to obtain the SCG signal, and the mastoid area at the head to obtain the BCG signal, respectively. For the distal reference points, we measure reflections from the right radial artery at the wrist and the right carotid artery at the neck. To measure PTT we use the aortic valve opening (AO) in the SCG waveform and the J-peak in the BCG waveform as the starting time reference points, while the foot of the pulse waveforms at the distal sites serves as the ending reference (Fig. 1d). By taking the time difference between pairs of these starting and ending reference points, our radar system is able to measure PTT across three different pairs: heart-to-wrist ($PTT_{SCG\rightarrow wrist}$), heart-to-neck ($PTT_{SCG\rightarrow neck}$) and head-to-wrist ($PTT_{BCG\rightarrow wrist}$). After measuring perturbations in PTT when the subject is at rest and following physical exercise, our system is able to derive an estimate of DBP along these pathways using a subject-specific calibration model[52].

Simultaneously measuring and isolating cardiac signals from multiple upper-body sites using a single radar system can be challenging for two key reasons. First, the physiological sites targeted by our system are small—the radial artery is 3 mm wide[42,53]. To achieve the necessary spatial precision, we leverage a high-resolution mmWave radar system (Texas Instruments AWR2243 Cascaded Radar RF Evaluation Module[54]), with 12 transmitters and 16 receivers, creating an effective array of 86 virtual antennas (Figure 1c). This configuration enables beamforming with an angular resolution of 1.4°. In contrast, prior systems[42,45,46] leverage smaller antenna arrays with 4–12 virtual antennas, limiting their angular resolution. Our signal processing pipeline then spatially decomposes the received signal into range-angle bins using range FFT and beamforming (Fig. 2a), applies a coarse spatial filter based on the known position of the participant and key physiological sites to classify signals as coming from the wrist, head, neck or heart. Finally, we design an adaptive bin ranking algorithm leveraging the autocorrelation properties, signal strength and periodicity, to prioritize signal bins containing the strongest cardiac pulse features.

Second, the received radar signal is a combination of reflections from multiple body regions, and environmental interference. As the pulse-induced displacements at distal arteries, such as the radial artery, are minute, approximately ≈30 μm[42,53], they can be overshadowed by noise sources within the radar's beam diameter such as minor muscle tremors at the wrist and neck and, respiratory motions at the heart which produce larger displacements of 1–4 mm[55].

To enable pulse transit time estimation in the presence of unwanted reflections, we design a DNN model to identify the periodic cardiac patterns in the radar signal and detect the timing of the key cardiac waveform features corresponding to the starting and ending timing reference for pulse transit time. The DNN model takes the phase and magnitude waveforms from the highest-ranked bins at the four key physiological sites as inputs, outputs a probability distribution of these signal features, and estimates PTT (Fig. 2c). Specifically, our DNN architecture consists of three key components: a spatial pooling block, a convolutional encoder-decoder architecture, and a cross-region fusion module.

Instead of relying only on the highest-ranked bins, we input a contiguous spatial region of bins centered around the four physiological sites to the DNN model. This design is motivated by the observation that the neighboring range and angle bins also contain valuable information as the pulse propagates across adjacent tissue regions. As the first DNN module to preprocess the radar signal, we design a spatial pooling block based on 1D Convolutional Neural Network (CNN) and Top-K spatial pooling filter to reduce the spatial dimensionality of the input waveforms.

To extract features from each region's waveforms we use a convolutional encoder-decoder architecture with U-Net skip connections[56] and a bi-directional long short-term memory (LSTM)[57] in between them for temporal modeling. This architecture captures both local waveform characteristics and longer temporal dependencies essential for accurate detection of cardiac waveform features.

Our network uses a cross-region fusion module based on attention layers that leverages the observation that cardiac signals at different body sites are likely to share common waveform characteristics as they originate from the same cardiac cycle. By fusing information across different measurement sites, our system is able to jointly estimate PTT across multiple sites, and is more resilient to noise or signal degradation at a single site.

Clinical testing

We conducted a human subjects study on 47 participants in an office environment on the Carnegie Mellon University campus (Table 1). Of

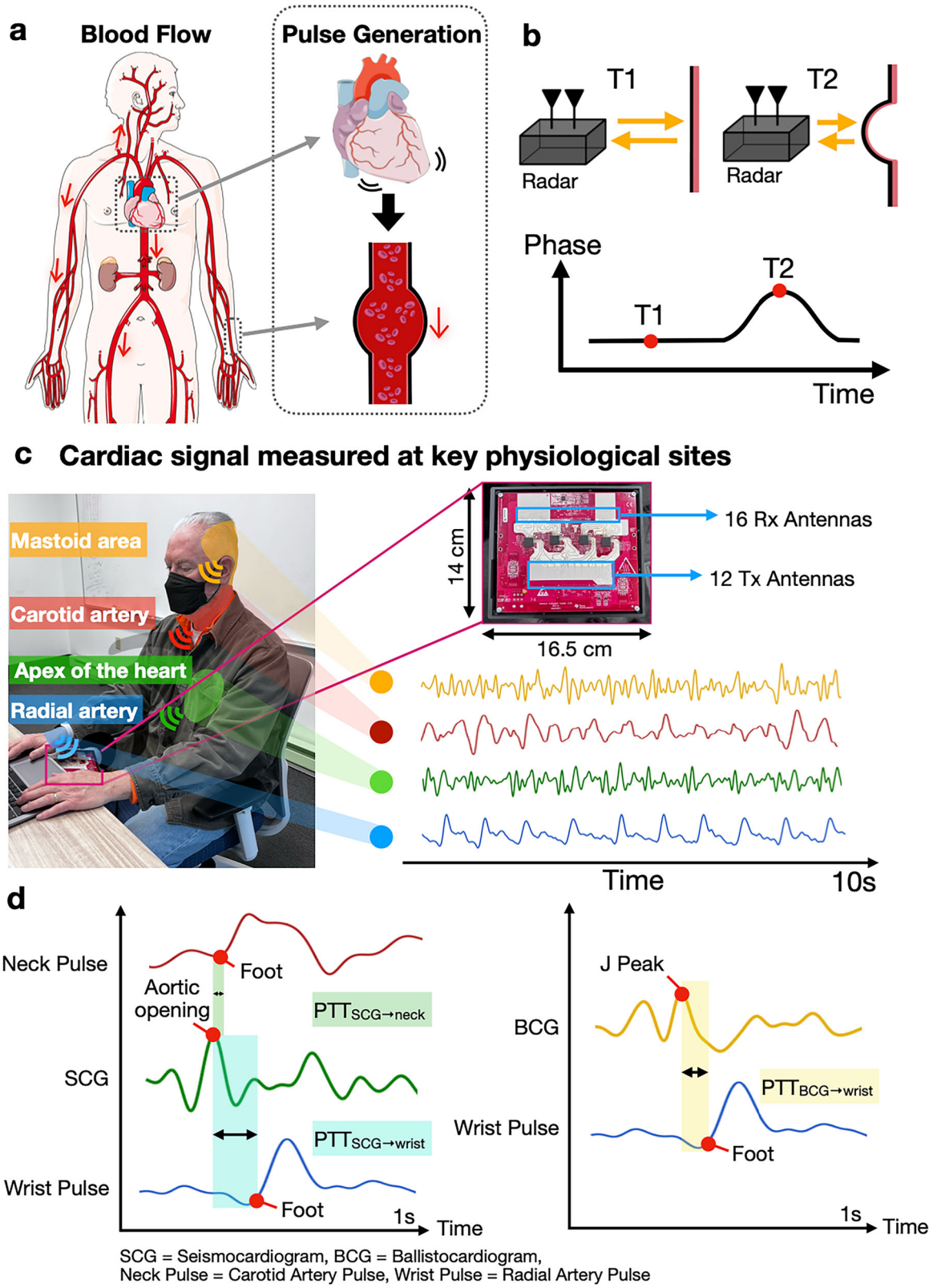

SCG = Seismocardiogram, BCG = Ballistocardiogram,
Neck Pulse = Carotid Artery Pulse, Wrist Pulse = Radial Artery Pulse

these participants, 6 participants had a high body mass index (BMI), defined as BMI >30 kg/m^2, 2 had atrial fibrillation, 2 had diabetes, 1 had bypass surgery and 6 had hypertension. Participants were recruited by word of mouth and an online platform for clinical study recruitment (Pitt+Me) with a mean age of 35 ± 16 years, height of 173.5 ± 8.6 cm, weight of 72.5 ± 15.8 kg, and female-to-male ratio of 0.47. All participants provided written informed consent prior to enrollment.

Participants sat upright in a chair positioned next to a table. The radar device was placed underneath the table, positioned ~10 cm below the wrist, and angled 10° towards the chest. This positioning resulted in the radar being ~50 cm from the chest and 65 cm from the neck and 70 cm from the head. Participants were instructed to rest their right arm on the table above the radar. To obtain a ground truth reference for PTT, contact-based IMU sensors were secured using

Fig. 1 | Overview of the mmWave radar system for multi-site pulse transit time (PTT) measurement. a Rhythmic contractions of the heart generate pulse waves that propagate across the arterial system. **b** The mmWave radar detects minute surface displacements by measuring phase variations in reflected signals over time. **c** The mmWave radar's beamforming algorithm targets four key physiological sites to measure PTT: the apex of the heart (green) and the mastoid area (yellow) as proximal reference points, and the radial artery (blue) and carotid artery (red) as distal arterial sites. The waveforms represent the phase signals from these sites, captured by the mmWave radar positioned at a fixed distance beneath the subject. **d** Our system estimates pulse transit time across three pairs: $PTT_{SCG\rightarrow wrist}$, $PTT_{SCG\rightarrow neck}$, $PTT_{BCG\rightarrow wrist}$. This is achieved by first identifying key cardiac waveform features: the aortic opening in the SCG signal, the J peak in the BCG signal, and the foot of the carotid and radial arterial pulse waveform. PTT is then computed as the time difference between these signal features at the proximal reference points and those at distal arterial sites. Heart and arterial circulation illustrations in (**a**) was adapted from Servier Medical Art (https://smart.servier.com), licensed under a Creative Commons Attribution 4.0 International License (https://creativecommons.org/licenses/by/4.0/).

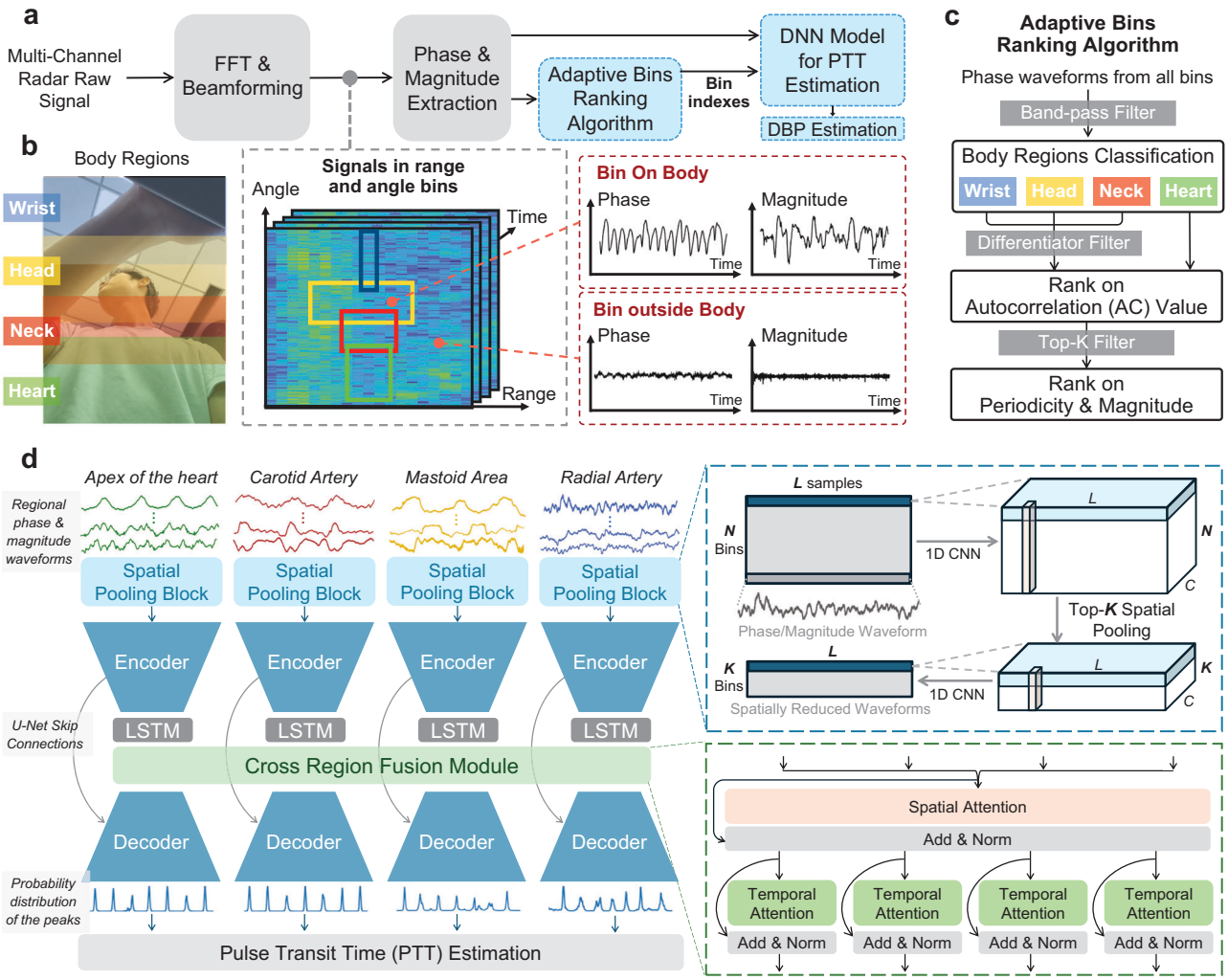

Fig. 2 | Signal processing and deep neural network pipeline to estimate PTT from mmWave radar reflections along multiple physiological pathways. a The system spatially decomposes the radar input channels into radar range and angular bins using FFT and beamforming. For each bin, phase and magnitude information are extracted. An adaptive bin ranking algorithm is applied to identify the bins with the strongest cardiac signal features, followed by a DNN model for PTT estimation. **b** Beamformed radar signal power is visualized across azimuth, range, and time axes, regions associated with higher signal power are brighter. Key physiological areas of interest, including the heart, neck, and wrist, are marked with bounding boxes that correspond to pre-defined search areas for a cardiac signal. The radar phase and magnitude from the key physiological sites show periodic signals corresponding to the cardiac cycle, while signals from non-physiological regions lack recognizable cardiac patterns. **c** Processing pipeline of the adaptive bin ranking algorithm. We leverage the pre-defined geometric constraints of the physiological sites, periodicity of the signal, and multi-step filtering to prioritize signal bins containing cardiac pulse features. **d** DNN architecture for multi-site PTT estimation. Our DNN architecture for PTT estimation employs a multi-branch design that jointly processes waveforms from four physiological sites (heart, neck, wrist, head) using three key components: Spatial Pooling Blocks for dimensionality reduction, Convolutional Encoder-Decoders with bi-directional LSTM for modeling the temporal relationship between cardiac waveform features, and Cross-region Fusion Modules that fuses correlated cardiac waveform features across different physiological sites.

straps at the apex of the heart, and the mastoid area behind the ear, and attached using medical tape at the base of the carotid artery above the left clavicle; a PPG sensor was affixed to the radial artery on the wrist using medical tape (Supplementary Fig. 1). The ground truth reference for blood pressure was obtained using a commercial blood pressure cuff (Omron BP7900[58]). Testing was conducted with participants wearing their regular clothing, which ranged from lightweight T-shirts to thicker sweaters.

https://doi.org/10.1038/s41467-026-73453-x

Table 1 | Demographic summary of participants in clinical study

	Age (years)	25.6 ± 6.2
	Height (cm)	175.4 ± 8.2
	Weight (kg)	73.0 ± 16.5
	BMI (kg/m^2)	23.6 ± 4.1
	Sex	
Development phase (n = 22)	Male, n (%)	17 (76)
	Female, n (%)	5 (24)
	Race	
	Asian, n (%)	22 (100)
	White, n (%)	0 (0)
	Black, n (%)	0 (0)
	Age (years)	43.5 ± 20.3
	Height (cm)	172.9 ± 9.0
	Weight (kg)	75.0 ± 15.5
	BMI (kg/m^2)	24.9 ± 4.9
	SBP at rest (mmHg)	122 ± 21
	DBP at rest (mmHg)	80 ± 12
Evaluation phase (n = 25)	Heart rate at rest (bpm)	72 ± 8
	Sex	
	Male, n (%)	15 (60)
	Female, n (%)	10 (40)
	Race	
	Asian, n (%)	11 (44)
	White, n (%)	13 (52)
	Black, n (%)	1 (4)
	Cardiovascular condition	
	Hypertension, n (%)	6 (24)
	AF, n (%)	2 (8)
	BPS, n (%)	1 (4)
	None, n (%)	16 (64)

BMI body mass index, *SBP* systolic blood pressure, *DBP* diastolic blood pressure, *AF* atrial fibrillation, *BPS* bypass surgery.

The study consisted of two phases: a development phase, during which data was collected to create the signal processing and neural network algorithms, and an evaluation phase, in which the system was prospectively tested on a new cohort of participants. Each participant's data collection session was divided into multiple measurements, with each measurement involving simultaneous recording of PTT using both the mmWave radar system and the contact-based reference sensors for three minutes. Between measurements, the contact-based sensor was removed and then reattached to the body. To induce large variations in PTT and BP, we had participants engage in an exercise protocol (Supplementary Fig. 2) that involved cardiopulmonary exercise by cycling on a stationary bike as dynamic exercises that require substantial metabolic demand are a commonly employed intervention that is known to trigger significant changes in PTT and BP[8].

During the training phase, we recruited healthy subjects (n = 22) with a mean age of 25.6 ± 6.2 years, height of 175.4 ± 8.2 cm, weight of 73.0 ± 16.5 kg, and female-to-male ratio of 0.29 (Table ??). A subset of participants (n = 10) completed a preliminary exercise protocol involving three measurements at rest, followed by five minutes of stationary cycling at 100% intensity, and three additional post-exercise measurements (Supplementary Fig. 2). The remaining participants (n = 14), including two subjects who participated in the preliminary protocol, underwent a full experimental protocol involving a wider range of exercise intensities (Supplementary Fig. 2). The full protocol began with two initial measurements at rest, followed by stationary cycling at sequentially adjusted exercise intensities, 50%, 75%, 100%, 75%, and 50%. Two measurements were taken between each exercise intensity level, with two final measurements at the conclusion of the protocol, resulting in 14 measurements in total for the full experimental protocol. Throughout all measurements, participants remained static while breathing normally.

In the evaluation phase of the study, participants (n = 25) were recruited both through Pitt+Me and by word of mouth at Carnegie Mellon University. These subjects completed the full experimental protocol, with blood pressure recorded at the beginning of each measurement using the commercial blood pressure cuff. The mean age of the subjects was 43 ± 21 years, with a mean height of 173.0 ± 9.1 cm, weight of 75.0 ± 15.5 kg, and a female-to-male ratio of 0.67 (Supplementary Table 2). In total, 279 sessions were used to evaluate PTT performance. After excluding sessions used for calibration, 195 sessions remained for DBP estimation. The PTT values computed by the mmWave radar system were compared against the contact-based reference sensors for the heart-to-wrist, heart-to-neck, and head-to-wrist physiological pathways. For each measurement, we use the median PTT value derived from both the mmWave radar system and reference sensors for evaluation. We note that we do not analyze the head-to-neck ($PTT_{BCG\to neck}$) pathway as the distance between the physiological points is substantially shorter than the other pathways. The correlation coefficient for $PTT_{SCG\to wrist}$, $PTT_{SCG\to neck}$, and $PTT_{BCG\to wrist}$ was R = 0.86, R = 0.76, and R = 0.75 respectively (Fig. 3a, c, e). The median absolute error for $PTT_{SCG\to wrist}$, $PTT_{SCG\to neck}$, and $PTT_{BCG\to wrist}$ was 6.7, 4.9, and 5.8 ms, respectively. Regarding the scale of PTT total variations (the differences between the maximum and minimum PTT measured by contact-based reference sensors), the relative median PTT errors for $PTT_{SCG\to wrist}$, $PTT_{SCG\to neck}$, and $PTT_{BCG\to wrist}$ were 12.3%, 10.5%, and 8.5%, respectively. Related works[59] leveraging ultra-wideband radar to compute PTT report mean errors of 56–58 ms, while related works[60] computing PAT (pulse arrival time), which is the sum of PTT and the pre-ejection period[8,10], report a median error of 33 ms.

Next, we evaluate our algorithm's ability to detect the key cardiac waveform features used to compute PTT: the aortic opening (AO) in the SCG signal, the J-peak in the BCG signal, and the waveform feet from the radial artery (wrist) and mastoid area (head). The median detection error was 10 ms for the aortic opening in the SCG signal, 14 ms for the J-peak in the BCG signal, and 12 ms and 14 ms for the waveform foot at the radial artery and the carotid artery, respectively. The higher detection error observed at the mastoid area correlates with the reduced performance of the $PTT_{BCG\to wrist}$ measurements compared to $PTT_{SCG\to wrist}$, as shown in Fig. 3. This performance difference can be attributed to the anatomical characteristics of the mastoid region, which has a larger surface area than other measurement sites, and is more susceptible to motion artifacts during seated measurements due to the head's distance from the body's center of mass.

To evaluate the repeatability of our system, we analyzed consecutive PTT measurements taken at rest prior to exercise intervention. For each subject, we compared the PTT values between two baseline measurements. The mean absolute difference (MAD) between successive measurements was 3.9 ± 1.7 ms for $PTT_{SCG\to wrist}$, 3.1 ± 2.3 ms for $PTT_{SCG\to neck}$, and 3.7 ± 2.1 ms for $PTT_{BCG\to wrist}$ across all participants. In comparison, the MAD between the measurements obtained from contact-based reference sensors were 3.3 ± 2.1 ms, 3.2 ± 3.0 ms, and 4.3 ± 4.1 ms, respectively. Prior work reports the mean and standard deviation of PTT fluctuations for subjects at rest is 14 ± 5 ms[61].

We also evaluated the performance of the mmWave radar system against a commercial blood pressure cuff at estimating diastolic blood pressure (DBP). To model the relationship between an individual's PTT

https://doi.org/10.1038/s41467-026-73453-x

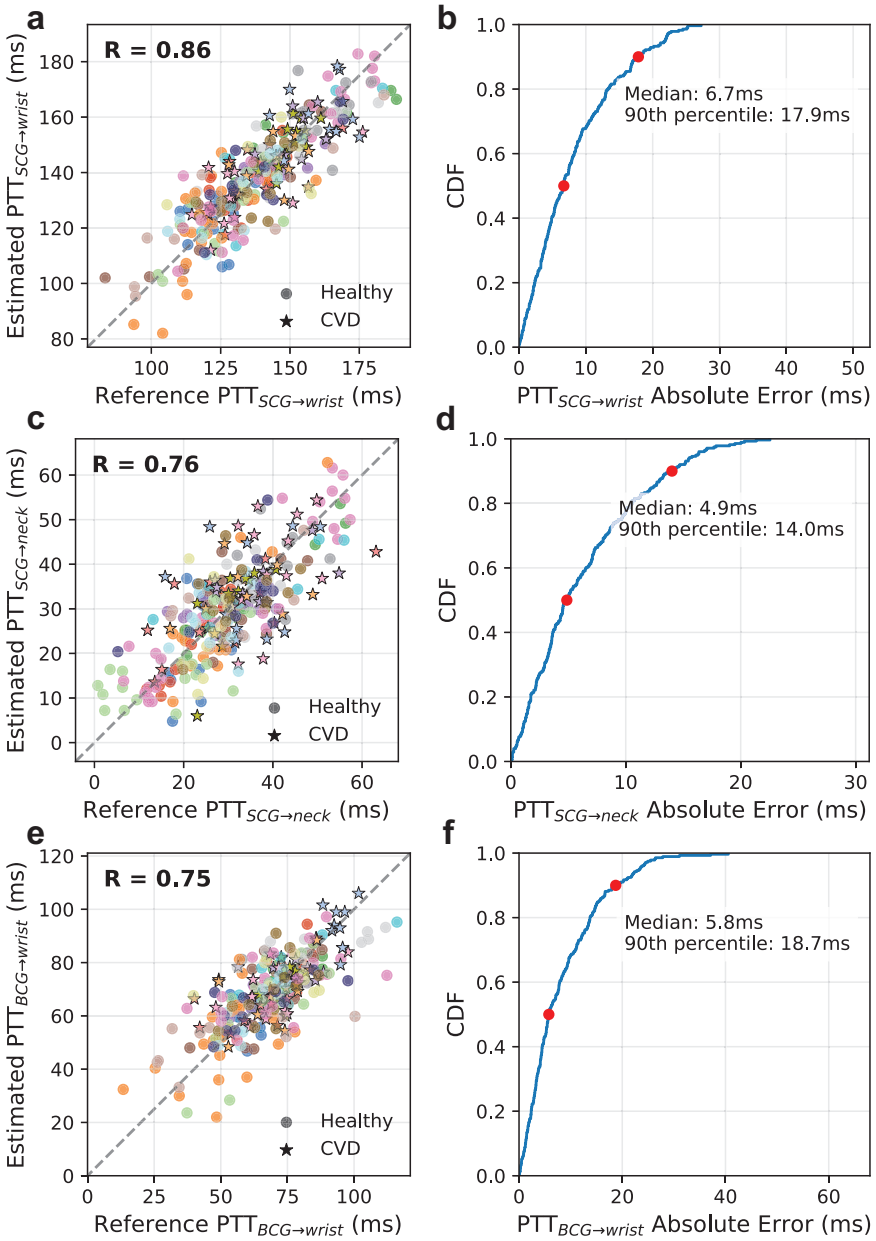

Fig. 3 | Comparison of PTT estimates from the mmWave radar system against contact-based reference sensors. a, **c**, **e** Correlation plots of PTT estimates and **b**, **d**, **f** Cumulative Distribution Function (CDF) plots of PTT errors for $PTT_{SCG→wrist}$, $PTT_{SCG→neck}$, and $PTT_{BCG→wrist}$. Data is shown for 25 participants (visualized in different colors) across 279 sessions in total.

measurements with DBP, we employed a subject-specific regression model[52] for calibration. For each participant, we used three recordings for calibration: one randomly selected resting-state measurement and two randomly selected post-exercise measurements. This randomization approach reduces selection bias and ensures the calibration captures a diverse range of physiological states. The correlation coefficient for DBP estimated from $PTT_{SCG→wrist}$, $PTT_{SCG→neck}$, and $PTT_{BCG→wrist}$ was R = 0.91, R = 0.90, and R = 0.90, respectively (Fig. 4a, c, e). Bland–Altman analysis[62] was performed for DBP estimated from $PTT_{SCG→wrist}$, $PTT_{SCG→neck}$, and $PTT_{BCG→wrist}$ and demonstrated a bias error of −0.62, 0.06, and −0.6 mmHg, respectively, with 7, 9, and 9 of 195 measurements falling outside the 95% agreement limits, respectively (Fig. 4b, d, f). The mean absolute error for DBP estimated by our radar system from $PTT_{SCG→wrist}$, $PTT_{SCG→neck}$, and $PTT_{BCG→wrist}$ was 3.50, 3.87, and 3.95 mmHg, respectively, while for the contact-based reference sensors the MAE was 3.33, 4.01, and 3.68 mmHg, respectively. Across these three PTT pairs, the MAE of our system is within −0.14–0.27 mmHg compared with the estimates derived from the contact-based reference sensors.

The DBP measurements derived from our radar system demonstrated performance that meets clinical guidelines for blood pressure monitoring devices. Our system achieved a mean error of −0.62, 0.06 and −0.60 mmHg and standard deviation of errors of 4.54, 4.98 and 5.20 mmHg based on estimates from $PTT_{SCG→wrist}$, $PTT_{SCG→neck}$, $PTT_{BCG→wrist}$, respectively. This is within the acceptable range of the FDA's Association for the Advancement of Medical Instrumentation guidelines for non-invasive sphygmomanometers[63], which allow mean errors up to 5 mmHg and standard deviation up to 8 mmHg. Furthermore, when assessed using the British Hypertension Society (BHS) criteria[64], our system's performance met the requirements for Grade A

https://doi.org/10.1038/s41467-026-73453-x

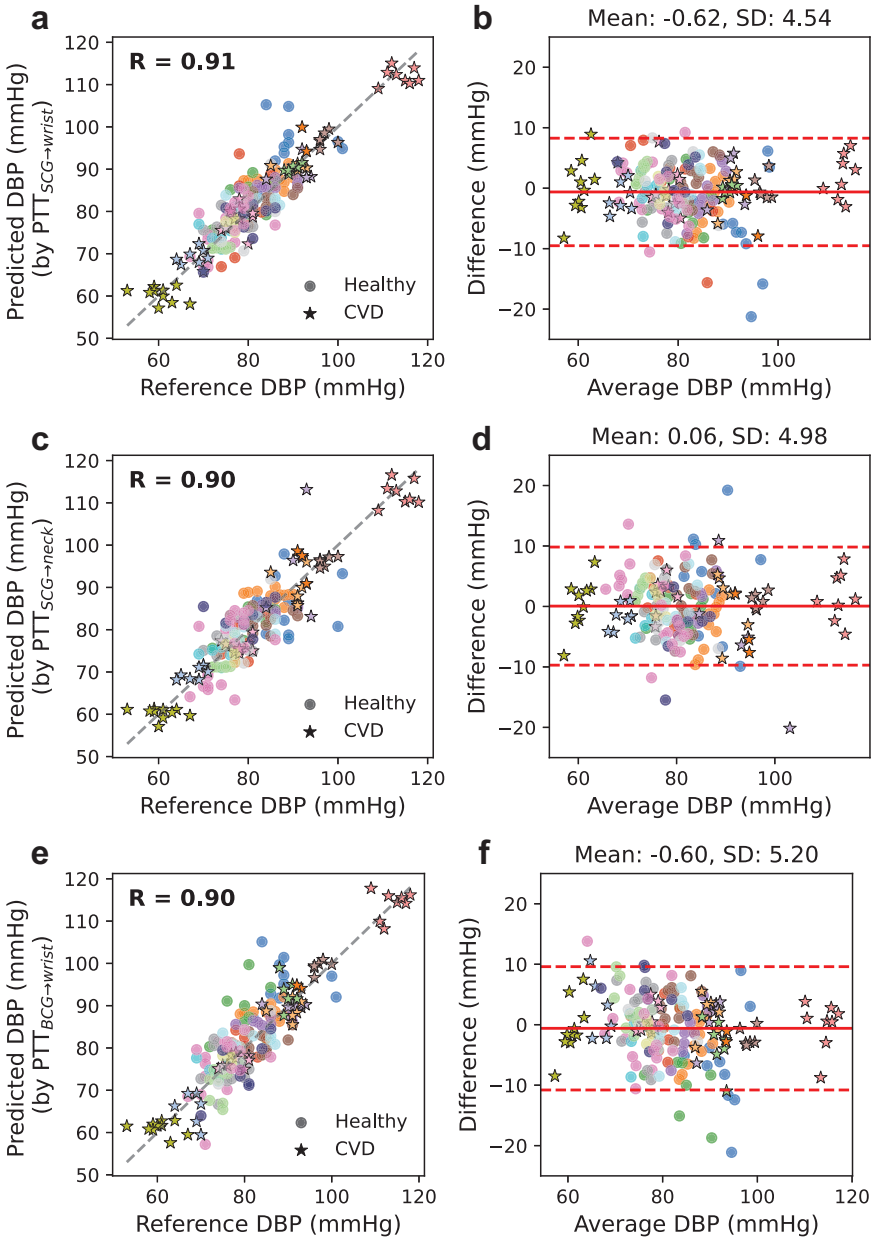

Fig. 4 | Comparison of diastolic blood pressure estimates from the mmWave radar system against a commercial blood pressure cuff. a, **c**, **e** Correlation plots and **b**, **d**, **f** Bland-Altman plots of DBP for $PTT_{SCG→wrist}$, $PTT_{SCG→neck}$, and $PTT_{BCG→wrist}$. Data is shown for 25 participants (visualized in different colors) across 195 sessions in total. In the Bland–Altman plot, the solid line represents the mean error and the dotted lines represent the 95% limits of agreement.

classification for all three PTT pairs (Supplementary Fig. 4). Specifically, 77.3%, 73.8%, and 69.6% of measurements had an error of ≤5 mmHg for the $PTT_{SCG→wrist}$, $PTT_{SCG→neck}$, and $PTT_{BCG→wrist}$ PTT pairs respectively; 98.0%, 95.8%, and 94.8% were within ≤10 mmHg; 98.5%, 98.4%, and 98.5% were within ≤15 mmHg. This performance achieves a Grade A classification requires that at least 60% of measurements be ≤5 mmHg, 85% be ≤10 mmHg, and 95% be ≤15 mmHg.

Subgroup analysis

We performed a subgroup analysis to evaluate the performance of our radar-based PTT measurement system across different demographic groups (Fig. 5).

For BMI subgroups, subjects with BMI≥28kg/m^2 showed median PTT errors of 7.4, 5.4, and 7.8 ms for the $PTT_{SCG→wrist}$, $PTT_{SCG→neck}$, and $PTT_{BCG→wrist}$, respectively. In comparison, subjects with 25–27.9 kg/m^2 demonstrated median errors of 5.5, 4.5, and 5.0 ms, respectively, while subjects with BMI ≤25 kg/m^2 showed median errors of 6.7, 4.6, and 5.5 ms, respectively, for the same PTT pairs.

For subjects with a height from 160 to 169 cm, the median error across the three cardiac pathways ranged from 3.6 to 5.0 ms. For the height group from 170 to 175 cm, the median error ranged from 4.3 to 5.4 ms, while for the group taller than 176 cm, the median error ranged from 4.8 to 6.9 ms across all pathways.

Comparison of PTT error by age subgroups show that subjects aged 18–25 years had median PTT errors of 6.3, 4.6, and 5.6 ms across the three PTT pairs. Subjects aged 26–60 years showed median errors of 6.6, 4.9, and 6.3 ms, while subjects greater than 60 years had median errors of 7.4, 5.4, and 5.8 ms, respectively.

When comparing PTT measurement performance by sex, female subjects demonstrated median errors of 5.7, 4.9, and 5.8 ms for the

https://doi.org/10.1038/s41467-026-73453-x

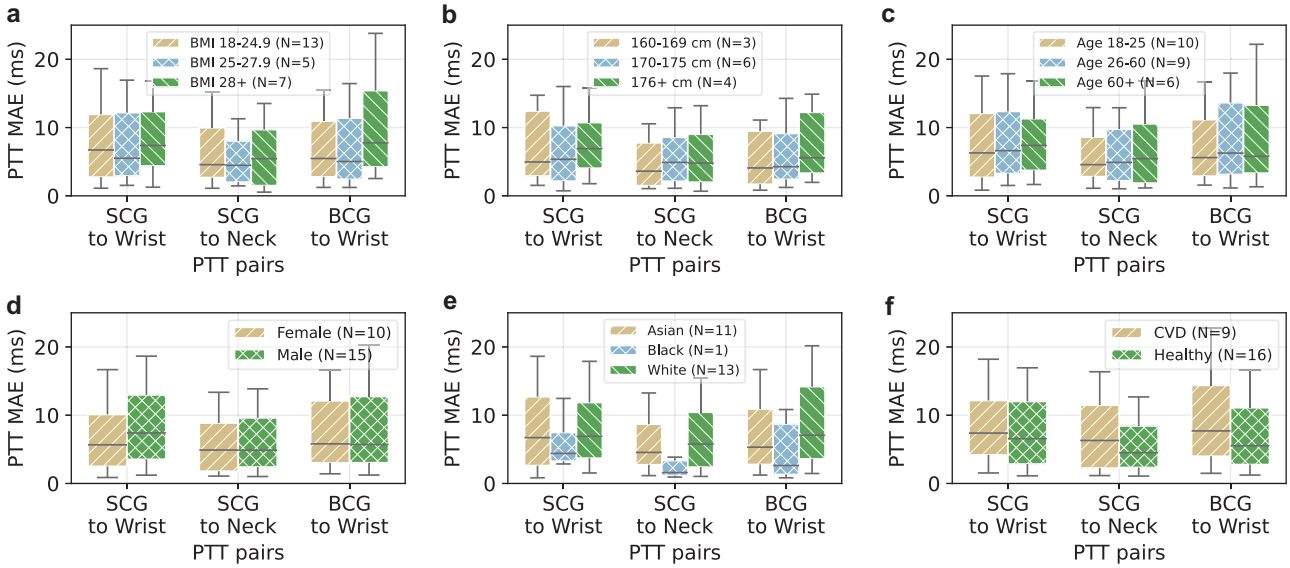

Fig. 5 | Subgroup analysis of PTT error across study participants. PTT Mean Absolute Error (MAE) for $PTT_{SCG\to wrist}$, $PTT_{SCG\to neck}$, and $PTT_{BCG\to wrist}$ across different **a** BMI ranges, **b** height ranges, **c** age ranges **d** female and male participants, **e** races, and **f** participants with and without cardiovascular conditions. Each box in the plots shows the median error (center line), 25th and 75th percentile errors (box edges), and 10th and 90th percentile errors (whiskers).

$PTT_{SCG\to wrist}$, $PTT_{SCG\to neck}$, and $PTT_{BCG\to wrist}$ PTT pairs, respectively. Male subjects showed median errors of 7.4, 4.9, and 5.7 ms, respectively, for the same PTT pairs.

Analysis by race indicated that Asian subjects had median PTT errors of 6.7, 4.6, and 5.3 ms across the three PTT pairs, respectively. The single Black subject in our cohort showed median errors of 4.4, 1.6, and 2.6 ms, respectively, while White subjects demonstrated median errors of 6.9, 5.8, and 7.1 ms, respectively.

Finally, we examined differences between subjects with cardiovascular disease (n = 9) and healthy subjects. Those with cardiovascular disease had median PTT errors of 7.4, 6.3, and 7.7 ms for the $PTT_{SCG\to wrist}$, $PTT_{SCG\to neck}$, and $PTT_{BCG\to wrist}$, respectively, while healthy subjects showed median errors of 6.6, 4.5, and 5.5 ms, respectively.

Ablation study of cross-region fusion module

To illustrate how simultaneous multi-site measurement enables our system to leverage correlated heartbeat variability across body sites to isolate noise, we conducted an ablation study comparing our full model, which includes the cross-region fusion module, against a variant in which the fusion module is removed and each physiological site is processed independently (n = 9 participants, 118 sessions). Without cross-region fusion, the model cannot exploit the shared cardiac cycle structure across sites to distinguish true pulse features from site-specific noise. With fusion enabled, the median absolute error for $PTT_{SCG\to wrist}$, $PTT_{SCG\to neck}$, and $PTT_{BCG\to wrist}$ was 5.2, 4.0, and 4.6 ms, respectively, compared to 10.3, 5.2, and 8.0 ms without fusion. The improvement was most prominent for pathways involving the wrist—median error decreased by 50% for $PTT_{SCG\to wrist}$ and 43% for $PTT_{BCG\to wrist}$—where the radial artery's small diameter of approximately 3 mm and susceptibility to muscle tremor artifacts can make it more challenging to detect pulse features from a single site in isolation. In contrast, $PTT_{SCG\to neck}$ showed a more modest improvement of 23%, consistent with the carotid artery producing a stronger and more easily detectable pulse signal.

We performed benchmark experiments on a single participant to evaluate the performance of our radar system across a range of experimental conditions and environmental scenarios (Fig. 6). We systematically evaluated design and environmental factors that could affect system accuracy, including the radar's distance to the participant, radar tilt angle, number of clothing layers, fidgeting movements by the participant, and different indoor environments. For each experimental setting, we collected measurements over 2–3 minutes and calculated the per-pulse median absolute PTT errors.

We varied the radar height from 5 to 60 cm below radial artery, as shown in Fig. 6a, to examine its effect on system performance. This was achieved by adjusting the height of the tripod on which the radar was mounted, directly changing the distance between the radar and the radial artery. Our evaluation shows that for the PTT pairs where the wrist is the distal site ($PTT_{SCG\to wrist}$, $PTT_{BCG\to wrist}$), the PTT error increased from 5.11 to 8.09 ms, and from 4.87 to 8.67 ms, respectively. In contrast, for $PTT_{SCG\to neck}$ the error exhibited a smaller increase from 3.57 to 5.28 ms.

We evaluate the effect of distance between the radar and the participant on system performance in the setup shown in Supplementary Fig. 3d. In this position, when the participant is away from the desk, the neck is the distal arterial point which is visible to the radar, and so we focus our evaluation on the $PTT_{SCG\to neck}$ pathway. As shown in Fig. 6b, the PTT errors were in the range of 3–5 ms, across the tested range of 0.50–2.25 m. This aligns with the operational distance of current commercial mmWave sensing devices[65].

We evaluated the effect of movements by the participant on system performance. As shown in Fig. 6c, across all PTT pairs, measurement errors were the lowest at 3.72–5.02 ms when the participant remained still. During common everyday movements such as talking or using a computer mouse, the PTT errors remained within a comparable range to that of the static condition. In the presence of fidgeting movements like arm shaking and head nodding, PTT errors increased to 3.82–7.64 ms. The largest PTT error of 9.52 ms was observed in the $PTT_{BCG\to wrist}$ pair during leg shaking. This is likely due to motion artifacts propagating through the body, and affecting multiple cardiac measurement points. In contrast, the $PTT_{SCG\to neck}$ pair showed the smallest error of 3–5 ms under motion, and was the least affected by fidgeting movements. We do note that related work measuring cardiac signals using active sonar[66], vision-based vibrocardiography[67], and inertial measurement units[68] also require users to remain static to obtain optimal results, as motion artifacts can mask subtle cardiac signals. Extending the system to work in the presence of natural user motions such as fidgeting would require designing motion tracking

https://doi.org/10.1038/s41467-026-73453-x

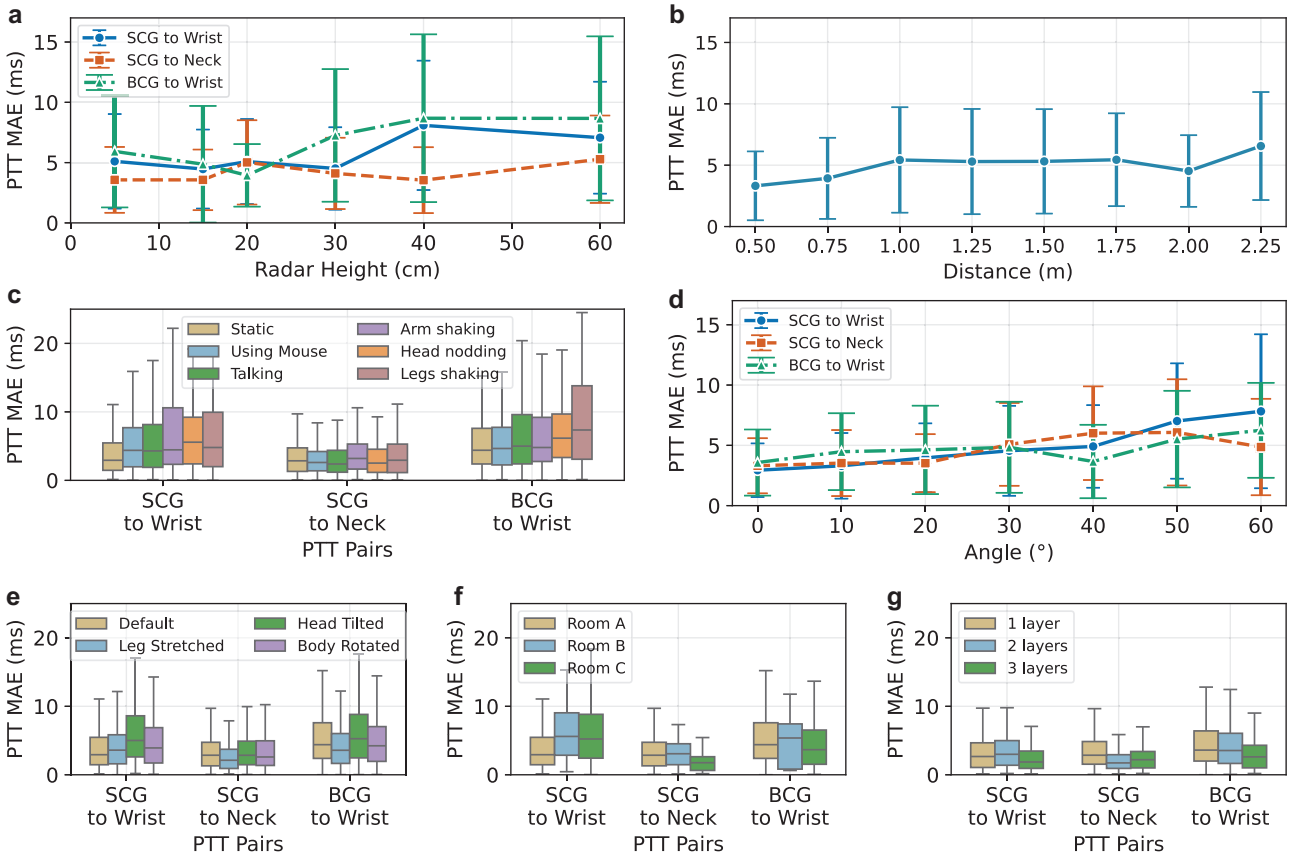

Fig. 6 | Benchmark testing across different scenarios. The system was evaluated under different **a** radar heights, **b** radar distances, **c** participant movements, **d** radar tilt angles, **e** participant postures, **f** testing environments, and **g** clothing layers. For the line plots in (**a**, **b**, **d**) markers, mean PTT mean absolute error (MAE); error bars, ±1 standard deviation (SD) of the pulse-level absolute errors. A total of 4 recording sessions, each 3 min in duration, were collected across the benchmark study. Each box includes 34–716 pulse-level data points, depending on the condition. For the box plots in (**c**, **e**, **f**, **g**) center line, median; box bounds, upper and lower quartiles (Q1 and Q3); whiskers, minimum and maximum values. Each box summarizes the distribution of pulse-level PTT MAE values for the corresponding condition.

and compensation algorithms capable of isolating cardiac signals from natural body movements.

We assessed the impact of varying the radar's tilt angle while keeping its height constant at 10 cm below the radial artery. Here, 0° corresponds to the radar facing upward towards the ceiling, and positive angles indicate a tilt toward the participant. The tilt angle was varied from 0° to 60° in increments of 10°. Figure 6d shows that all three PTT pairs exhibit similar trends, with measurement errors becoming larger as the tilt angle increases. Errors remained below 5 ms for all PTT pairs at angles up to 30° and increased to 6.07–7.82 ms at 60° across all pairs. This is likely due to stronger signal reflections from the wrist and neck at smaller tilt angles.

We evaluated the effect of different natural sitting postures. These scenarios involve the participant tilting their head, stretching a leg, or rotating their torso to simulate common movements during sedentary activities. As shown in Fig. 6e, measurement errors across all PTT pairs ranged from 2.44 to 6.05 ms under these postural variations. Compared to the initial static posture, these posture-induced variations had modest to minimal impact on system performance.

We assessed the system performance in different indoor environments. Fig. 6f shows that the system consistently maintained PTT errors below 5 ms across multiple indoor locations, relative to Room A, where the main study was performed. This indicates that the system's performance remains stable across different indoor environments.

We investigated the impact of the number of clothing layers on system performance by having subjects wear one, two, or three layers of indoor clothing, as illustrated in Fig. 6g. Starting from the second clothing layer onwards, both the wrist and neck positions were fully covered by clothing. The resulting PTT errors stayed below 5 ms for all three layers, suggesting consistent performance despite additional clothing layers. This is consistent with prior work[41] that shows mmWave signals can penetrate fabric and measure cardiac signals. We note that related systems that leverage optical or laser sensing technologies[33,38] to measure cardiac signals, can only operate effectively on exposed skin, while acoustic sensing technologies[66] to measure heart rhythms are limited to penetrating only a single layer of clothing.

We evaluated system performance over a 12-month monitoring period. As shown in Fig. 7a, PTT measurement errors across the three arterial pathways, $PTT_{SCG\to wrist}$, $PTT_{SCG\to neck}$, and $PTT_{BCG\to wrist}$ changed from 7.94 ± 6.87 ms to 7.66 ± 6.34 ms, 4.18 ± 3.33 ms to 7.67 ± 6.08 ms, and 8.27 ± 8.51 ms to 7.05 ± 8.36 ms for each pathway, respectively. Fig. 7b illustrates DBP estimation performance over the same period. The MAE remained below 5 mmHg after 12 months without and with recalibration, achieving Grade A classification per the BHS standard[64]. Recalibrating the model at Month 12 yielded improved DBP estimation performance errors across the arterial pathways, $PTT_{SCG\to wrist}$, $PTT_{SCG\to neck}$, and $PTT_{BCG\to wrist}$, from 2.9 ± 2.0 mmHg to 2.5 ± 2.5 mmHg, 3.4 ± 2.4 mmHg to 2.8 ± 2.5 mmHg, and 4.8 ± 3.7 mmHg to 3.0 ± 3.0 mmHg, respectively. Future studies are required to evaluate changes in system performance at more granular time intervals and across longer time scales.

https://doi.org/10.1038/s41467-026-73453-x

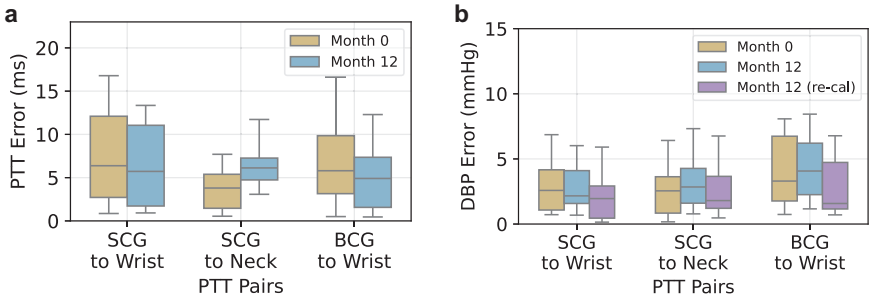

Fig. 7 | System performance across time. a PTT measurement error across three arterial pathways at month 0 and month 12. **b** DBP mean absolute error at month 0, and at month 12 without and with recalibration. $n = 2$ participants were evaluated in this longitudinal study. Each box includes 28 sessions. For the box plots in (**a**, **b**) center line, median; box bounds, upper and lower quartiles (Q1 and Q3); whiskers, minimum and maximum values. Each box summarizes the distribution of errors for the corresponding condition.

Discussion

This work presents a system to measure multi-point pulse transit time and diastolic blood pressure using a single radar. Prior work[69–72] on BP estimation using PTT has largely focused on measuring a single PTT pair from the heart to distal sites including the finger, ear, or forehead. However, BP estimates obtained through each of these pairs may not be equivalent due to differences in hemodynamic controls, which affect vessel characteristics and blood distribution at different sites[73]. Simultaneous multi-site PTT measurement can enable a more comprehensive assessment of pathway-specific dynamics, by capturing differences between central and peripheral stiffness, which have been proposed as markers of arterial health and associated with mortality risk[17,18,20–22]. Our contactless approach streamlines these measurements with a single radar without repositioning the device, while allowing the user to remain seated upright. This eliminates the need for whole-body sensor attachment and can reduce measurement time and complexity. Further studies would be required to assess its effects on diagnostic outcomes of cardiovascular disease.

While blood pressure provides a standardized measure of cardiovascular health, prior work[19] has noted the value in measuring PTT alone. A marked decrease in an individual's PTT compared to their baseline could be indicative of cardiovascular risk. As such, PTT alone has been proposed as a risk marker for remote monitoring of individuals at risk of cardiac events.

Our work is focused on comparing the relationship between PTT and DBP as prior work suggests that arterial stiffness and vascular tone, key factors affecting PTT, correlate more strongly with DBP than SBP[9,74]. Our system leverages cardiac waveform foot-detection methods, which have also been shown to correlate with changes in DBP[9]. We note that related studies using contact-based methods measure pulse arrival time (PAT), which measures the time interval between the ECG R peak and peripheral pulse points, is empirically more closely correlated with SBP[74,75].

The systolic and diastolic blood pressure estimation errors, obtained after calibration using a regression model best fitted for each subject across a subset of evaluation dataset, are presented in Supplementary Fig. 5. For DBP, the radar system achieved a mean absolute error (MAE) of 2.62 ± 0.82 mmHg for $PTT_{SCG \to wrist}$ and 2.55 ± 0.73 mmHg for $PTT_{SCG \to neck}$, comparable to the contact-based reference sensors which demonstrated MAEs of 2.26 ± 0.54 mmHg and 2.36 ± 0.58 mmHg, respectively (Supplementary Fig. 5a, e). For systolic blood pressure (SBP), both radar-based and contact-based approaches exhibited higher errors. The radar system yielded MAEs of 7.08 ± 2.79 mmHg for $PTT_{SCG \to wrist}$ and 6.84 ± 3.00 mmHg for $PTT_{SCG \to neck}$, while the contact-based sensors reported MAEs of 6.47 ± 2.38 mmHg and 6.32 ± 2.76 mmHg, respectively (Supplementary Fig. 5b, f). The cumulative distribution function (CDF) plots (Supplementary Fig. 5c, g) indicate that the error distributions for SBP estimation remain comparable between the radar system and the contact-based sensors across the entire error range. In addition, Supplementary Fig. 5d, h shows the correlation between the SBP estimates of the contact-based sensors and our radar system against the blood pressure cuff. The SBP correlation coefficient for $PTT_{SCG \to wrist}$ and $PTT_{SCG \to neck}$ was $R = 0.86$ and $R = 0.87$, respectively, for our radar system, which is similar to the contact-based sensors with $R = 0.90$ and $R = 0.89$, respectively.

Our system has the following limitations. First, our current design focuses on measuring physiological sites on the upper body. We do note however that our system can in principle measure the cardiac signal at arterial points on the lower body such as the femoral artery which exhibits a pulse-induced skin displacement of ~200 µm, which is similar to that of the carotid artery[76]. Extending the system to simultaneously measure arterial points on both the upper and lower body is a goal for future work and would require hardware modifications—such as increased transmission power and additional antennas along the elevation axis. These additions would not only enable whole-body pulse detection but could also accommodate a broader range of user postures beyond the current seated configuration.

Second, our clinical study included a limited number of subjects with cardiovascular conditions, specifically, six participants had diagnosed hypertension and two had atrial fibrillation. While subgroup analysis did not reveal any significant differences in PTT errors between healthy participants and those with CVD, future studies are required to assess the performance of our system across a larger number of participants with cardiovascular disease and related health conditions that affect PTT and DBP.

Third, our system's performance is constrained by the accuracy of the reference devices used in this study. Future studies could compare against established clinical measures of arterial stiffness such as pulse wave velocity through applanation tonometry or cuff-based systems (SphygmoCor XCEL, AtCor Medical[77]), peripheral arterial tonometry (EndoPAT 2000, Itamar Medical[78]), and catheter-based reference measurements.

Fourth, our study uses a simple linear model to estimate DBP from PTT measurements. We show in Supplementary Fig. 6 and Supplementary Table 3 that using logarithmic and inverse quadratic models produce comparable results. However, more complex models and calibration procedures could be used to take into account physiological factors such as cardiac output and vascular tone as well as conditions such as stress[8,79–82].

Finally, our proof-of-concept system was implemented on an mmWave evaluation board with an approximate cost of $4400. While this development platform was selected to enable rapid prototyping, in a commercial version of our design, the core algorithms would be integrated into a PCB design with a lower cost, which mirrors the development trajectory of commercial mmWave systems.

In summary, we present a proof-of-concept system that demonstrates the feasibility of leveraging mmWave radar for multi-site estimates of PTT and DBP. Given the increasing prevalence of mmWave radar technology, our approach has the potential to enable a more accessible means of monitoring cardiovascular health without cuffs or contact-based sensors. Future studies are needed to validate the system across a broader patient population and across longer time scales.

Methods

Study design

This study was approved by Carnegie Mellon University's Institutional Review Board (STUDY2024_00000342). All studies complied with relevant ethical regulations. Participants were recruited by word of mouth from the Carnegie Mellon University student community and via Pitt+Me from the general public in Pittsburgh PA, USA. Written consent was obtained for human subjects participating in the study. Sex was self-reported by participants. Participant received $30 Amazon gift card per visit. All demographic and clinical data are reported in aggregate to ensure participant anonymity. Randomization was not applicable and investigators were not blinded.

Healthy participants above the age of 18 were eligible for the study. Exclusionary criteria include pregnant women and nursing mothers. Participants were screened via inclusion and exclusion criteria prior to the study.

Measurement setup

The mmWave radar contains a 2D array of 12 transmitter antennas with T_θ = 9 and T_ψ = 3 antennas in the azimuth and elevation angle, respectively, and 16 receiver antennas with R_θ = 16 antennas in the azimuth angle, respectively. After eliminating duplicate virtual antenna locations, a total of 86 virtual antennas remain. The radar transmits at a power of 13 dBm (20 mW), which is within the typical range for Wi-Fi routers[83]. The radar was mounted on a tripod positioned approximately 10 cm below the wrist and angled 10° toward the chest.

Measuring cardiac signals using mmWave radar

The mmWave radar transmits a chirp with linearly increasing frequency from f_0 = 77 GHz to f_1 = 81 GHz where the detailed radar configuration can be found in Supplementary Table 1. The received signal contains reflections from the human body, which capture the subtle changes in the distance between the antenna and the body, which are modulated by the cardiac signals. However, as the received signal is a combination of reflections from different parts of the body, which contain multiple cardiac signals and motion, as well as changes in the environment, we next spatially decompose the reflections into different range and angle bins, and identify the bin corresponding to the physical location where a target cardiac signal is the strongest.

Algorithm to localize cardiac signals

The goal of this step is to spatially isolate reflections caused by a target cardiac signal and minimize interference from other cardiac signals and motion from the body, as well as environmental sources. The localization process involves four steps:

Signal spatial isolation. To extract cardiac-related reflections, we leverage FMCW radar processing to decompose signals based on their distance and use beamforming to separate signals based on their angle. The FMCW radar continuously transmits chirp signals with linearly increasing frequency. The receiving antennas capture the reflected signal from objects in the environment and mix the transmitted signal to produce the intermediate frequency (IF) signal. The transmitted signal $x_{\mathrm{TX}}(\tau)$ and received signal $x_{\mathrm{RX}}(\tau)$ at time τ within a chirp period T can be formulated as $x_{\mathrm{TX}}(\tau) = A_{\mathrm{TX}} \cdot e^{j(2\pi f_0 \tau + \frac{\pi B}{T}\tau^2)}$ and $x_{\mathrm{RX}}(\tau) = A_{\mathrm{RX}} \cdot e^{j(2\pi f_0(\tau - t_d) + \frac{\pi B}{T}(\tau - t_d)^2)}$ where A_{TX} and A_{RX} denote the signal amplitude of transmitted and received signals, f_0 is the starting frequency, B is the bandwidth, and t_d is the round-trip time delay between transmitting and receiving. The IF signal $x(\tau)$ is obtained by mixing the received signal with the conjugate of the transmitted signal, given by $x(\tau) = x_{\mathrm{RX}}(\tau)x^*_{\mathrm{TX}}(\tau)$. The analog-to-digital converter on the radar is configured to sample N points per chirp, where the discrete time is given by $t = \frac{N\tau}{T}$. By applying the Fast Fourier Transform (FFT) in the discrete-time domain $\mathcal{F}$, we obtain the frequency components $X_n = \mathcal{F}[x[t]]$, where n indicates the range bin index from 0 to N.

In addition to separating reflections by range, we apply receiver-side beamforming to spatially isolate reflections in the angular dimension. Specifically, for a radar system with multiple receiving antennas, we perform a spatial FFT across the antenna array to separate reflections along the azimuth angle. This process is expressed as $X_{n,\theta} = \mathcal{F}[X_n[r]]$, where θ represents the azimuth angle bin index, and r is the index of the receiving antenna.

Localizing using known anatomical constraints. We leverage our knowledge of human anatomy and the relative positioning of the radar to constrain our search space for cardiac signals. Based on our experimental setup with the radar positioned below the subject's body, we can spatially map the relevant anatomical regions as shown in Fig. 2.

In the configuration, the distance between the radar and the wrist, heart, neck, and head is 10, 50, 65, and 70 cm, respectively. We configure the radar with N = 128 samples per chirp, yielding a range resolution of 4.22 cm. This allows us to define specific range bins for each anatomical target: $n_{wrist} \in [4.22, 16.88]$ cm for the radial artery, $n_{heart} \in [37.98, 54.86]$ cm for the apex of the heart, $n_{carotid} \in [50.64, 67.52]$ cm for the carotid artery, and $n_{mastoid} \in [59.08, 75.96]$ cm for the mastoid area. Similarly, by applying FFT in the azimuth dimension with a size of 128, we achieve an angular resolution of 1.4°. This allows us to constrain the angular search space enough to specific sectors for each anatomical target: $\theta_{wrist} \in [-20, 20]^\circ$ for the radial artery, $\theta_{heart} \in [-60, -20]^\circ$ for the apex of the heart, $\theta_{carotid} \in [-40, 0]^\circ$ for the carotid artery, and $\theta_{mastoid} \in [-35, 5]^\circ$ for the mastoid area.

These anatomically informed constraints reduce the search space substantially, allowing our system to focus on regions most likely to contain the cardiac signals of interest while filtering out irrelevant reflections from other body regions or the environment.

Identifying periodic signals. The goal in this step is to identify the range and angle bin where the periodicity of a target cardiac signal is maximized. To do this, we first compute the phase values $\phi_{n,\theta}[t]$ for each range and angle bin. Next, we apply a bandpass filter on the phase signals to remove breathing and body motion artifacts, using different frequency ranges for each measurement site: 0.5–100 Hz at the wrist, 0.5–10 Hz at the heart and neck, and 0.7–4 Hz at the head. We then detrend[84] the phase signal to remove linear trends and center it at zero. Furthermore, we apply the differentiator filter[85,86] to sharpen the cardiac waveform features from the heart and neck.

Next, we compute the autocorrelation function (ACF) of the phase signal in all range and angular bins to detect repeating patterns that reflect the periodic nature of the cardiac cycle: $ACF[m] = \sum_{t=0}^{C} \phi_{n,\theta}[t]\phi_{n,\theta}[t+m]$, where C is the number of chirps in the recording and m is the time lag. The ACF quantifies how well the signal aligns with a time-shifted version of itself. We extract the peaks in the ACF where the time lag is greater than zero, denoted as $[p_1, p_2, \ldots, p_i, \ldots]$ at lags $[lag_1, lag_2, \ldots, lag_i, \ldots]$. For each bin, we calculate the maximum magnitude of the peaks in the ACF with time lags correspond to the typical frequency range of the heart rhythm, i.e. lag_i/f_s is in the range of 0.7–3 Hz (48–180 bpm) where f_s is the number of chirps per second. We then sort the bins based on the magnitudes to identify the signal with the strongest periodicity.

Filtering interference from non-cardiac reflections. We observe that while the top bin selected in the previous step has the strongest periodicity, it may not be due to the target cardiac signal, but may be due to interference from periodic reflections.

To identify the bin where the SCG, BCG and carotid artery signal originates, we select the top 40 bins and re-rank them based on signal power. Since the signal from target area exhibits prominent displacement, the bin with the highest power is identified as the most likely source of the signal.

To identify the bin where the radial pulse originates, our goal is to discard outlier bins that capture periodic reflections that do not correspond to the cardiac signal. To do this, we record lag_i for the top 40 bins computed in the previous step. Using a histogram with a fixed bar size of 10 data points, we identify the most frequent lag value. We then select the bin that also shares the most common lag value.

DNN model to compute pulse transit time

Problem formulation. To estimate the PTT between two different body sites, we develop a temporal detection model to detect the exact timing of the key cardiac waveform features in each desired site: the aortic opening (AO) in the SCG signal, the J-peak in the BCG signal, and the waveform foots from the radial artery (wrist) and mastoid area (head). Once the key features are identified, the PTT between two sites can be derived by calculating the time differences. Given the beamformed signal $X_{n,\theta}[t] \in \mathbb{C}^{N\times\Theta\times T}$, where N, Θ, T are the number of range bins, angles bins, and chirps, respectively. We seek to learn a classification model f_i for site i: $f_i(X_{n,\theta}[1], X_{n,\theta}[2], \ldots, X_{n,\theta}[T]) = (y[1], y[2], \ldots, y[T])$, where $y[t] \in \{0, 1\}$ indicates if the timestamp t has a key cardiac waveform feature, labeled using contact-based reference sensors. Instead of designing a DNN directly for binary classification, we apply label smoothing[87] to estimate a continuous probability distribution for the key features. Specifically, we replace the binary labels at the locations of the key features with a Gaussian kernel centered at the feature's location with a maximum value of 1 and a standard deviation of 10. This formulation transforms our approach from binary classification to a temporal continuous regression model. This Gaussian representation provides more informative gradients during training, resulting in more robust model convergence than sparse binary labels.

With the range bin $\hat{n}_i$ and angle bin $\hat{\theta}_i$ with the strongest cardiac signal from site i identified in previous steps, we use a contiguous spatial region of bins centered around $(\hat{n}_i, \hat{\theta}_i)$ as the inputs to the DNN. Specifically, we use 21 angle bins for heart, neck, wrist, and 5 range bins ×21 angle bins for head. We flatten the range and angles bins for head region into a single dimension. For each bin, we calculate the magnitudes and unwrapped phases (i.e. $|X_{n,\theta}[t]|$ and $\angle X_{n,\theta}[t]$) of the complex numbers, concatenate them in the spatial dimension and use as the inputs to the DNN. Given a total number of B_i bins around site i, the model f_i can be denoted as $f_i : \mathbb{R}^{2B_i\times T} \to \mathbb{R}^T$.

Loss function. We employ binary cross entropy as our loss function to train the temporal detection model. For each site i, the loss $\mathcal{L}_i$ is computed between the predicted probability sequence $\hat{y}_i[t]$ and the Gaussian-smoothed ground truth $y_i[t]$:

$$\mathcal{L}_i = -\frac{1}{T}\sum_{t=1}^{T}\left[y_i[t]\log(\hat{y}_i[t]) + (1-y_i[t])\log(1-\hat{y}_i[t])\right] \quad (1)$$

For our joint model that simultaneously detects the key cardiac features across all four body sites, the total loss is the sum of individual site losses (i.e. $\mathcal{L}_{\text{total}} = \sum_i \mathcal{L}_i$, where $i \in \{heart, neck, wrist, head\}$)

Spatial pooling block. We consider a region of neighboring angle and ranges bins as the inputs of DNN since they contain valuable information as the arterial pulse propagates across the adjacent tissue region. To reduce the spatial dimensionality and suppress the noise in the raw phase and magnitude waveforms, we design a spatial pooling block as the preprocessing module of the DNN. For each body site i, we input waveforms from $2B_i$ spatial bins (phase and magnitude) of length T samples, forming input tensor $X \in \mathbb{R}^{2B_i\times T}$. This input is processed through two consecutive 2D convolutional layers with kernel size (1, 7) and padding (0, 3) to preserve temporal resolution. Each layer produces 16 feature maps followed by batch normalization and ReLU activation, yielding $X' \in \mathbb{R}^{16\times 2B_i\times T}$. We then apply Top-$K$ spatial pooling, which selects the K features with the highest values across the spatial dimension, reducing dimensions to $X'' \in \mathbb{R}^{16\times K\times T}$ where $K < B_i$. The K values are set to $K_{heart} = 8$, $K_{neck} = 8$, $K_{head} = 16$, and $K_{wrist} = 4$ for the respective sites. Finally, a 1 × 1 convolution layer projects the channel dimension from 16 down to 1, producing output $\tilde{X} \in \mathbb{R}^{K\times T}$ where the spatial dimension has been effectively reduced from $2B_i$ to K bins. This design distills the most relevant spatial information while maintaining sensitivity to temporal patterns in the cardiac waveform.

Convolutional encoder-decoder. After spatial pooling, we implement a U-Net style convolutional encoder-decoder architecture to extract temporal features and generate sample-level probabilities of key features. The encoder consists of three consecutive blocks, each containing two 1D convolutional layers (kernel size = 7) with batch normalization and ReLU activation, followed by max pooling with stride 2. The channel dimensions progressively increase from K to [32, 64, 128] to capture hierarchical features while downsampling the temporal dimension. At the bottleneck, we employ a bidirectional LSTM with 2 layers, 64 hidden units, and dropout rate of 0.2 to model long-range temporal dependencies in the signal. The decoder mirrors the encoder with three blocks that use transposed convolutions with a stride 2 for upsampling, concatenate with corresponding encoder features via skip connections, and process through two 1D convolutional layers with batch normalization and ReLU. These skip connections preserve fine-grained temporal details that might otherwise be lost during downsampling. The final output passes through two additional convolutional layers with a sigmoid activation function, producing a probability distribution $\hat{y}_i[t] \in [0, 1]^T$ for each timestamp. This architecture remains consistent across all four body sites, differing only in the input spatial dimension K from the spatial pooling block.

Cross-region fusion module. Since pulse waves at different anatomical sites originate from the same cardiac cycle, they can exhibit temporal correlations with similar waveform features[88]. However, signal quality can vary across sites due to local tissue properties and measurement conditions. To exploit these relationships, we implement a cross-region fusion module between the encoder and decoder stages, after the bottleneck LSTM processes each site's feature independently. Operating on feature representations with hidden size 128, the module employs a dual attention mechanism with 4-head multi-head attention. First, cross-site attention allows each site's features to incorporate relevant information from other sites, followed by residual connections and layer normalization. Then, temporal attention is applied to each site independently, enabling focus on temporally significant patterns. This architecture enables the network to jointly model spatial relationships between anatomical sites and temporal dynamics within each site, making the system more resilient to local noise and improving PTT estimation accuracy by leveraging complementary information across all measurement sites.

Dataset preprocessing. We randomly divide the evaluation phase participants (n = 13) into two equal sets. To evaluate the performance on set 1 participants, we train the model using all development phase participants plus set 2 evaluation participants, and vice versa for

evaluating on set 2. Each radar measurement session lasts 80–110 s. We define each data sample as a 5-s segment of radar data, using a sliding window approach with a 1-s stride. This process generates ~10.8 k samples from development phase participants, 3.0 k samples from evaluation set 1, and 3.1 k samples from evaluation set 2.

Data augmentation. To improve model robustness and generalization, we implement a spatial bin dropout augmentation strategy. During training, instead of using all available spatial bins B_i for each site i, we randomly select a subset of $B\prime_i$ bins in every new epoch. Specifically, we use $B\prime_{head} = 75$ (out of 105 bins), $B\prime_{neck} = 35$ (out of 42 bins), and $B\prime_{heart} = 30$ (out of 42 bins), with no augmentation for wrist. This technique forces the model to learn from different spatial combinations, preventing it from over-relying on specific bins that might have strong signals in the training data but could be less reliable in real-world scenarios. Additionally, this form of augmentation acts as a regularization mechanism to reduce overfitting and improve the model's ability to handle variable signal quality. During validation and testing phases, we use all available bins to maximize performance.

Training procedure. We employ a two-stage training strategy with the AdamW optimizer. In the first stage, we train the network for each individual site without cross-region fusion, using 20% of the training data for validation. The site-specific hyperparameters are: batch size of 128 and learning rate of 0.001 for all sites, with weight decay of 0.01 for head and wrist networks and 0.0001 for heart and neck networks. We train each site-specific network for 50 epochs. In the second stage, we freeze all site-specific components and train only the cross-region fusion module with a batch size of 36, learning rate of 0.0004, weight decay of 0.0001, and for 30 epochs. This two-stage approach allows us to first build strong site-specific feature extractors and then optimize their integration.

Deriving PTT from DNN output. To extract pulse transit times from the probability distributions of the key features produced by our model, we employ a multi-step post-processing approach. First, we identify significant peaks in the probability sequences using a peak detection algorithm with a minimum distance constraint of 300 ms between consecutive peaks and site-specific height thresholds (0.55 for heart, 0.5 for neck, 0.25 for wrist, and 0.35 for head). Once peaks are detected across all sites, we calculate PTT values between pairs of sites by taking the time difference between corresponding peaks, constraining the values to physiologically plausible ranges. To ensure measurement stability, we apply outlier removal by excluding PTT values with z-scores exceeding 2.0, followed by temporal smoothing using a moving average filter with a kernel size of 5. This processing pipeline effectively translates the model's probabilistic outputs into PTT measurements over time.

PTT performance evaluation. Our radar system adjusts its focus to enhance the detection of stronger cardiac signals, whereas the contact-based reference sensors remain fixed at predetermined anatomical locations throughout the measurement process. This difference in positioning introduces a spatial discrepancy between the radar's target site and the exact placement of the reference sensors. For instance, when measuring at the neck, the contact-based sensor is positioned over the carotid artery just above the clavicle, while the radar targets a segment of the carotid artery located ~10 cm higher at the upper neck. Given that the pulse wave velocity typically ranges from 5 to 10 m/s[89], and assuming a constant propagation speed between the reference sensor and the radar's measurement site, this 10 cm displacement results in a time shift of ~10–20 ms. To assess the performance of radar-based PTT, we prioritize the analysis of dynamic variations rather than absolute values. Therefore, we normalize the PTT values obtained from the contact-based sensor by aligning their mean with the mean of the radar-derived PTT measurements, effectively eliminating this constant temporal offset. This normalization ensures a fair comparison of PTT fluctuations between the two modalities, as illustrated in Fig. 3.

Estimating diastolic blood pressure from PTT. Several methods have been proposed for calibrating PTT with blood pressure[34]. We select the linear regression model $DBP = a \cdot PTT + b$[52], which is computationally efficient, requires fewer data points, and is widely used in PTT-BP calibration.

In our blood pressure evaluation (Fig. 4, Supplementary Fig. 5), we calibrate the regression model using three data points per subject. To ensure sufficient variability in the data, one point is randomly selected when the subject is at rest, while the other two are randomly chosen from post-exercise measurements. This approach enhances the robustness of the calibration by incorporating a range of physiological states.

Ground truth reference measurement setup

Contact-based reference sensors. To obtain a reference measurement of pulse transit time, we use the accelerometer of an inertial measurement unit (Seeed Studio XIAO nRF52840 Sense[90]), and a PPG sensor (Electronics LLc, PulseSensor[91]) to measure the cardiac signals at different points along the body. The IMU is configured to have a sampling rate of 416 Hz with a linear acceleration sensitivity of 0.061 mg/LSB[92], and the PPG sensor is configured to have a sampling rate of 500 Hz. We resample the IMU data to 500 Hz to make it consistent with the sampling rate of PPG and the rate of chirps of radar.

Sensor synchronization. In our measurement setup (Supplementary Fig. 1), an IMU and PPG sensor is packaged in a plastic case and attached to the radial artery of the subject's right wrist and an IMU is attached to the carotid artery of neck above right clavicle using transparent wound dressing (Dimora Transparent Film[93]), while other two IMUs are attached to the apex of heart and mastoid area of the head using an elastic band[94] and velcro strap design[95]. All reference sensors are connected via a USB cable to a laptop for recording. The IMU and PPG at the wrist are connected to the same clock and synchronized. As the four IMU reference sensors (IMU_{wrist}, IMU_{head}, IMU_{heart}, IMU_{neck}) each have a different clock, we perform a calibration step at the beginning of each measurement to synchronize the sensor data across them and the mmWave radar. Following common practice[96–99] in kinematic research, we time-synchronize our reference sensors using a prominent mechanical perturbation, performed as deliberate shaking events of the sensors in unison.

Step 1. We attach the IMU_{neck} to the participant's neck.

Step 2. We attach the PPG_{wrist} and IMU_{wrist} to the participant's wrist.

Step 3.IMU_{head} and IMU_{heart} are shaken up and down along the y-axis for two seconds.

Step 4.IMU_{head} is attached to the head band.

Step 5.IMU_{heart} is held with IMU_{neck} and shaken up and down along the y-axis for two seconds.

Step 6.IMU_{heart} is held with IMU_{wrist} and shaken up and down along the y-axis for two seconds.

Step 7.IMU_{heart} is attached to the chest band.

Step 8.IMU_{wrist} is placed ~10 cm from the mmWave radar and shaken up and down towards the device and along the y-axis for two seconds.

To synchronize the signals, we identify the time window across a signal pair that contains the shaking motion, and use that window to compute the time lag between the recordings. To do this, we leverage a sliding window approach that segments the signal pairs into windows

of duration [*wlen*, *wlen* + *step*] where *wlen* = 2*s* and *step* = 0.02*s*. For all window pairs, we perform cross-correlation between the two windows and find the amplitude of the maximum peak. Intuitively, the window containing shaking would contain the highest cross correlation peak because due to the synchronized shaking motion. Outside of the period of shaking, the sensors move independently and show minimal correlation. For the time window when shaking occurs, the time lag of the maximum peak is used to synchronize the signals.

We next synchronize IMU_{wrist} with the mmWave radio data. We first constrain the shaking motion of wrist is 30 cm above radar. Then we select radar with the angle bin from −36 ° to 20 ° with the corresponding range bin. We then apply differentiator filter[85,86] on radar phase signal to align the radar signal characteristic with IMU signal. Next, we perform the same synchronization algorithm among IMU sensors with each pair of IMU_{wrist} and radar range-angle bins. Finally, we select the time lag of the maximum peak with the largest peak value among selected radar bins.

Computing pulse transit time from reference sensors

We use the PPG sensor at the wrist as a reference measure of the pulse at the radial artery, the z-axis from IMU_{neck} as a reference measure of the pulse at the carotid artery, the x-axis from IMU_{head} as a reference measure of BCG, and the z-axis from IMU_{heart} as a reference measure of SCG.

Using our reference sensors, the *i*th PTT measurement is computed as the interval between the start of the pulse t_i^{start} and its arrival at a peripheral arterial site t_i^{end}. In our system, we can compute the proximal point of PTT on the timing of the aortic valve opening (AO) from the SCG signal at time, or the J peak in the BCG signal. We compute the distal point of PTT at a peripheral site using the foot of the PPG signal at the radial artery at the wrist and the primary peak of the IMU signal (the foot of pulse distension) at the carotid artery at the neck[100]. Of these two signal types (IMU, PPG), we find that the pulse waveform captured via the PPG sensor exhibits the highest SNR. As such, we first search for t_i^{end} in the PPG signal at the wrist, then search for the corresponding t_i^{start} and t_i^{end} in the SCG, BCG, and neck pulse signal relative to it.

Identifying $t_i^{end}[Wrist]$ at wrist from PPG signal. The t_i^{end} of each pulse in the wrist PPG signal occurs at the foot of each cardiac cycle and is minimally affected by wave reflection[8]. While previous works have proposed various definitions for the foot location in a single cadiac cycle[8,101,102], we use the intersecting tangent method to identify the foot point. To perform this peak selection across multiple recorded cardiac cycles, we first apply a low-pass filter with a cutoff frequency of 10 Hz to remove noise artifacts. We then compute the first derivative of the waveform to identify the point of maximum gradient. Finally, we determine the intersection of the horizontal line at the local minimum with the tangent at the maximum gradient point to find the desired foot location.

Identifying t_i^{start} and t_i^{end} from IMU signals. Next, we search for the corresponding t_i^{start} for SCG BCG signals and t_i^{end} for carotid artery signal at neck. In the SCG signal, this is the aortic valve opening time, while in the BCG signal we use the J peak, which has been shown to have a stronger correlation with blood pressure when calculating PTT from BCG to wrist PPG[31]. In the carotid artery signal, we find the first major peak following the Start of Isovolumetric Contraction (SIC). In the absence of noise, the AO peak in the SCG waveform, the J peak in the BCG signal and the major peak after SIC at the carotid artery signal are typically the highest amplitude features in the signal. However, challenges arise due to the sensitivity of the IMU signal to motion artifacts, variations in sensor placement, and differences in BMI among subjects. Consequently, the highest measured peak within a cardiac cycle may not always correspond to the target peaks. To tackle this challenge, we first perform a broad search with the reference PPG foot time $t_i^{end}[Wrist]$ for candidate time points to avoid selecting noise outside the *PTT* range. Then we perform a refined search to avoid selecting neighboring peaks that obscure the desired target peaks.

Broad search for peaks in IMU signals. In this step, we search for candidate time points within periodically increasing search windows of sizes ranging from $w_{\min} = 100ms$ to $w_{\max} = 300ms$. We set the initial search window of $[t_i^{end}[Wrist] - w, t_i^{end}[Wrist]]$, where $w = w_{min}$, and progressively move the starting point backwards in time until $w = w_{\max}$. The intuition for this approach is to exclude peaks resulting from unintended movements outside the expected PTT range.

We mark the timestamp of the maximum amplitude peak within the time windows as the candidate peak $\widetilde{t_{i,w}}$ within the SCG, BCG, or carotid artery signal. We then sum the amplitudes of all candidate peaks in the time windows a measure of the amount of vibration energy, which we illustrate for the SCG signal: $S[w] = \sum_{w=w_{\min}}^{w_{\max}} \sum_{i=0}^{P} SCG[\widetilde{t_{i,w}}]$. We then find the window size which maximizes the sum of the amplitudes of the candidate starting peaks in the signal: $w^* = \arg\max_w(S)$. We then set the coarse-grained starting time to be $\widetilde{t_i} = \widetilde{t_{i,w^*}}$.

Refined search for t_i. Next we refine our estimate of the candidate starting time $\widetilde{t_i}$. The intuition behind this approach is that the majority of target peaks are found correctly with the window size w^*. To minimize the selection of neighboring peaks that may correspond to noise, we identify the most likely PTT value while applying a small threshold to ensure robustness to local PTT variance. To do this, we mark the timestamp with the maximum peak amplitude within the refined search window $[(t_i - w^*) - \delta, (t_i - w^*) + \delta]$ as the final selected t_i value where the threshold $\delta = 30$ ms.

Software. Data from the mmWave radar was collected using mmWave Studio (v03.00.00.14, Texas Instruments). IMU and PPG sensor data were collected using custom Python (v3.11.9) scripts via serial communication. Signal processing of radar IQ data was performed using custom MATLAB (R2023a, MathWorks) scripts. Machine learning models were trained and evaluated using PyTorch (v2.4) in Python (v3.11.9). Figures were created using matplotlib (v3.9.2).

Reporting summary

Further information on research design is available in the Nature Portfolio Reporting Summary linked to this article.

Data availability

The processed example sensor data (anonymized subset) generated in this study have been deposited in Zenodo under accession code 10.5281/zenodo.19403782. The raw radar and wearable sensor recordings generated in this study are protected and are not available due to participant privacy under the IRB-approved study protocol.

Code availability

All custom code generated in this study is publicly available at https://github.com/ZJendex/polypulse-pttunder the MIT License.

References

1. Boutouyrie, P. et al. Pharmacological modulation of arterial stiffness. *Drugs* **71**, 1689–1701 (2011).
2. Safar, M. E. Arterial stiffness as a risk factor for clinical hypertension. *Nat. Rev. Cardiol.* **15**, 97–105 (2018).
3. Mattace-Raso, F. U. et al. Arterial stiffness and risk of coronary heart disease and stroke: the Rotterdam study. *Circulation* **113**, 657–663 (2006).

4. Katz, E. S., Lutz, J., Black, C. & Marcus, C. L. Pulse transit time as a measure of arousal and respiratory effort in children with sleep-disordered breathing. *Pediatr. Res.* **53**, 580–588 (2003).
5. Pitson, D. & Stradling, J. Value of beat-to-beat blood pressure changes, detected by pulse transit time, in the management of the obstructive sleep apnoea/hypopnoea syndrome. *Eur. Respir. J.* **12**, 685–692 (1998).
6. Hughes, T. M., Craft, S. & Lopez, O. L. Review of 'the potential role of arterial stiffness in the pathogenesis of Alzheimer's disease'. *Neurodegener. Dis. Manag.* **5**, 121–135 (2015).
7. Smith, R. P., Argod, J., Pépin, J.-L. & Lévy, P. A. Pulse transit time: an appraisal of potential clinical applications. *Thorax* **54**, 452–457 (1999).
8. Mukkamala, R. et al. Toward ubiquitous blood pressure monitoring via pulse transit time: theory and practice. *IEEE Trans. Biomed. Eng.* **62**, 1879–1901 (2015).
9. Wang, E. J. et al. Seismo: Blood pressure monitoring using built-in smartphone accelerometer and camera. In *Proceedings of the 2018 CHI Conference on Human Factors in Computing Systems* (ACM, 2019).
10. Geddes, L., Voelz, M., Babbs, C., Bourland, J. & Tacker, W. Pulse transit time as an indicator of arterial blood pressure. *Psychophysiology* **18**, 71–74 (1981).
11. Peter, L., Noury, N. & Cerny, M. A review of methods for non-invasive and continuous blood pressure monitoring: pulse transit time method is promising? *Irbm* **35**, 271–282 (2014).
12. Foo, J. & Wilson, S. Clinical applications of pulse transit time in paediatric critical care. *J. Med. Eng. Technol.* **33**, 79–86 (2009).
13. Bahache, M., Lemayian, J. P., Wang, W. & Hamamreh, J. M. An inclusive survey of contactless wireless sensing: A technology used for remotely monitoring vital signs has the potential to combating COVID-19. *RS Open J. Innov. Commun. Technol.* **1**, https://doi.org/10.46470/03d8ffbd.5b3676f3 (2020).
14. van den Bosch, H. C. et al. Site-specific association between distal aortic pulse wave velocity and peripheral arterial stenosis severity: a prospective cardiovascular magnetic resonance study. *J. Cardiovasc. Magn. Reson.* **17**, 2 (2015).
15. Beeckman, S. et al. Heart-carotid pulse-wave velocity via laser-doppler vibrometry as a biomarker for arterial stiffening: a feasibility study. *Physiol. Meas.* **46**, 045006 (2025).
16. Manoj, R., Raj, K. V., Nabeel, P. M., Sivaprakasam, M. & Joseph, J. titleMeasurement of pressure dependent variations in local pulse wave velocity within a cardiac cycle from forward travelling pulse waves. *Sci. Rep.* **15**, 3066 (2025).
17. Stone, K. et al. The aortic-femoral arterial stiffness gradient: an atherosclerosis risk in communities (ARIC) study. *J. Hypertens.* **39**, 1370–1377 (2021).
18. Fortier, C. et al. Aortic-brachial stiffness mismatch and mortality in dialysis population. *Hypertension* **65**, 378–384 (2015).
19. Di Rienzo, M., Avolio, A., Rizzo, G., Zeybek, Z. M. I. & Cucugliato, L. Multi-site pulse transit times, beat-to-beat blood pressure, and isovolumic contraction time at rest and under stressors. *IEEE J. Biomed. Health Inform.* **26**, 561–571 (2021).
20. Troitskaya, E. A., Velmakin, S. V., Goreva, L. A. & Kobalava, Z. D. Aortic-brachial stiffness mismatch as potential marker of subclinical arterial damage in patients with rheumatoid arthritis. *RUDN J. Med.* **27**, 167–181 (2023).
21. Jin, L. et al. Uncoupling of the center-to-periphery arterial stiffness gradient and pulse pressure amplification in viral pneumonia infection. *BMC Infect. Dis.* **23**, 657 (2023).
22. Curcio, R. et al. Serum myostatin is associated with central-to-peripheral arterial stiffness gradient in healthy adolescents: the maciste study. *Am. J. Hypertens.* **37**, 777–783 (2024).
23. Kemmotsu, O. et al. Arterial tonometry for noninvasive, continuous blood pressure monitoring during anesthesia. *Anesthesiology* **75**, 333–340 (1991).
24. Allen, J. & Murray, A. Age-related changes in peripheral pulse timing characteristics at the ears, fingers and toes. *J. Hum. Hypertens.* **16**, 711–717 (2002).
25. Wang, H. et al. Quantitative comparison of the performance of piezoresistive, piezoelectric, acceleration, and optical pulse wave sensors. *Front. Physiol.* **10**, 1563 (2020).
26. Holz, C. & Wang, E. J. Glabella: Continuously sensing blood pressure behavior using an unobtrusive wearable device. In *Proceedings of the ACM on Interactive, Mobile, Wearable and Ubiquitous Technologies* (ACM, 2017).
27. Carek, A. M., Conant, J., Joshi, A., Kang, H. & Inan, O. T. SeismoWatch: wearable cuffless blood pressure monitoring using pulse transit time. In *Proceedings of the ACM on Interactive, Mobile, Wearable and Ubiquitous Technologies* (ACM, 2017).
28. Carek, A. & Holz, C. Naptics: convenient and continuous blood pressure monitoring during sleep. In *Proceedings of the ACM on Interactive, Mobile, Wearable and Ubiquitous Technologies* (ACM, 2018).
29. Ganti, V. G. et al. Wearable cuff-less blood pressure estimation at home via pulse transit time. *IEEE J. Biomed. Health Inform.* **25**, 1926–1937 (2020).
30. Winokur, E. S., Da He, D. & Sodini, C. G. A wearable vital signs monitor at the ear for continuous heart rate and pulse transit time measurements. In *2012 Annual International Conference of the IEEE Engineering in Medicine and Biology Society*, 2724–2727 (IEEE, 2012).
31. Yousefian, P. et al. The potential of wearable limb ballistocardiogram in blood pressure monitoring via pulse transit time. *Sci. Rep.* **9**, 10666 (2019).
32. Salvi, P. et al. Validation of a new non-invasive portable tonometer for determining arterial pressure wave and pulse wave velocity: the PulsePen device. *J. Hypertens.* **22**, 2285–2293 (2004).
33. Niu, L. et al. Full-body cardiovascular sensing with remote photoplethysmography. In *Proceedings of the IEEE/CVF Conference on Computer Vision and Pattern Recognition*, 5994–6004 (IEEE, 2023).
34. Murakami, K., Yoshioka, M. & Ozawa, J. Non-contact pulse transit time measurement using imaging camera, and its relation to blood pressure. In *2015 14th IAPR International Conference on Machine Vision Applications (MVA)*, 414–417 (IEEE, 2015).
35. Huang, Y. et al. Camera-based blood pressure monitoring based on multi-site and multi-wavelength pulse transit time features. In *IEEE Transactions on Instrumentation and Measurement* (IEEE, 2024).
36. Patil, O. R., Wang, W., Gao, Y. & Jin, Z. A camera-based pulse transit time estimation approach towards non-intrusive blood pressure monitoring. In *2019 IEEE International Conference on Healthcare Informatics (ICHI)*, 1–10 (IEEE, 2019).
37. Block, R. C. et al. Conventional pulse transit times as markers of blood pressure changes in humans. *Sci. Rep.* **10**, 16373 (2020).
38. Beeckman, S. et al. Enhancing multichannel laser-doppler vibrometry signals with application to (carotid-femoral) pulse transit time estimation. In *2023 45th Annual International Conference of the IEEE Engineering in Medicine & Biology Society (EMBC)*, 1–7 (IEEE, 2023).
39. Antolinos, E., Pérez-Fernández, F. N. & Grajal, J. Pulse wave velocity monitoring using a mmwave radar network. In *2023 IEEE MTT-S International Microwave Biomedical Conference (IMBioC)*, 85–87 (IEEE, 2023).

40. Singh, L., You, S., Jeong, B. J., Koo, C. & Kim, Y. Remote estimation of blood pressure using millimeter-wave frequency-modulated continuous-wave radar. *Sensors* **23**, 6517 (2023).
41. Geng, F. et al. Contactless and continuous blood pressure measurement according to caPTT obtained from millimeter wave radar. *Measurement* **218**, 113151 (2023).
42. Liang, Y. et al. airBP: Monitor your blood pressure with millimeter-wave in the air. *ACM Trans. Internet Things* **4**, 1–32 (2023).
43. Johnson, J., Kim, C. & Shay, O. Arterial pulse measurement with wearable millimeter wave device. In *2019 IEEE 16th International Conference on Wearable and Implantable Body Sensor Networks (BSN)*, 1–4 (IEEE, 2019).
44. Yoshioka, M. & Bounyong, S. Analysis of pulse transit time derived from imaging photoplethysmography and microwave sensor-based ballistocardiography. In *Proceedings of the IEEE/CVF Conference on Computer Vision and Pattern Recognition Workshops*, 286–287 (IEEE,2020).
45. Hu, Q. et al. Contactless arterial blood pressure waveform monitoring with mmWave radar. In *Proceedings of the ACM on Interactive, Mobile, Wearable and Ubiquitous Technologies* (ACM, 2024).
46. Cao, Y., Zhang, S., Li, F., Chen, Z. & Luo, J. hbp-fi: Contactless blood pressure monitoring via deep-analyzed hemodynamics. In *IEEE INFOCOM 2024-IEEE Conference on Computer Communications*, 1211–1220 (IEEE, 2024).
47. Escobar-Restrepo, B., Torres-Villa, R. & Kyriacou, P. A. Evaluation of the linear relationship between pulse arrival time and blood pressure in ICU patients: potential and limitations. *Front. Physiol.* **9**, 1848 (2018).
48. Payne, R., Symeonides, C., Webb, D. & Maxwell, S. Pulse transit time measured from the ecg: an unreliable marker of beat-to-beat blood pressure. *J. Appl. Physiol.* **100**, 136–141 (2006).
49. Podrug, M. et al. What is the smallest change in pulse wave velocity measurements that can be attributed to clinical changes in arterial stiffness with certainty: a randomized cross-over study. *J. Cardiovasc. Dev. Dis.* **10**, 44 (2023).
50. Townsend, R. R. et al. Recommendations for improving and standardizing vascular research on arterial stiffness: a scientific statement from the American Heart Association. *Hypertension* **66**, 698–722 (2015).
51. Sharma, P., Imtiaz, S. A. & Rodriguez-Villegas, E. Acoustic sensing as a novel wearable approach for cardiac monitoring at the wrist. *Sci. Rep.* **9**, 20079 (2019).
52. Wibmer, T. et al. Pulse transit time and blood pressure during cardiopulmonary exercise tests. *Physiol. Res.* **63**, 287–296 (2014).
53. Giannattasio, C. et al. Arterial stiffening influence of sympathetic nerve activity: evidence from hand transplantation in humans. *Hypertension* **45**, 608–611 (2005).
54. mmWave cascade imaging radar RF evaluation module https://www.ti.com/tool/MMWCAS-RF-EVM (2024).
55. Pedersen, A. N., Korreman, S., Nyström, H. & Specht, L. Breathing adapted radiotherapy of breast cancer: reduction of cardiac and pulmonary doses using voluntary inspiration breath-hold. *Radiother. Oncol.* **72**, 53–60 (2004).
56. Ronneberger, O., Fischer, P. & Brox, T. U-net: Convolutional networks for biomedical image segmentation. In *Medical image computing and computer-assisted intervention–MICCAI 2015: 18th international conference, Munich, Germany, October 5-9, 2015, proceedings, part III 18*, 234–241 (Springer, 2015).
57. Yu, Y., Si, X., Hu, C. & Zhang, J. A review of recurrent neural networks: LSTM cells and network architectures. *Neural Comput.* **31**, 1235–1270 (2019).
58. Healthcare, O. *Complete Blood Pressure Monitor + EKG, Model BP7900: Instruction Manual*. Omron Healthcare, Inc. https://omronhealthcare.com/. (2023).
59. Cho, H.-S. & Park, Y.-J. Measurement of pulse transit time using ultra-wideband radar. *Technol. Health Care* **29**, 859–868 (2021).
60. Buxi, D., Redouté, J.-M. & Yuce, M. R. Blood pressure estimation using pulse transit time from bioimpedance and continuous wave radar. *IEEE Trans. Biomed. Eng.* **64**, 917–927 (2016).
61. Drinnan, M. J., Allen, J. & Murray, A. Relation between heart rate and pulse transit time during paced respiration. *Physiol. Meas.* **22**, 425–432 (2001).
62. Bland, J. M. & Altman, D. Statistical methods for assessing agreement between two methods of clinical measurement. *Lancet* **327**, 307–310 (1986).
63. ANSI/AAMI/ISO 81060-2:2018 non-invasive sphygmomanometers—part 2: Clinical investigation of intermittent automated measurement type. https://www.iso.org/standard/73339.html. (2018).
64. O'Brien, E. et al. The British Hypertension Society protocol for the evaluation of automated and semi-automated blood pressure measuring devices with special reference to ambulatory systems. *J. Hypertens.* **8**, 607–619 (1990).
65. Gruzewska, E. et al. UWB radar-based heart rate monitoring: A transfer learning approach. Preprint at https://arxiv.org/abs/2507.14195 (2025).
66. Wang, A., Nguyen, D., Sridhar, A. R. & Gollakota, S. Using smart speakers to contactlessly monitor heart rhythms. *Commun. Biol.* **4**, 1–12 (2021).
67. Yan, B. P. et al. Contact-free screening of atrial fibrillation by a smartphone using facial pulsatile photoplethysmographic signals. *J. Am. Heart Assoc.* **7**, e008585 (2018).
68. Da He, D. *A Wearable Heart Monitor at the Ear Using Ballistocardiogram (BCG) and Electrocardiogram (ECG) with a Nanowatt ECG Heartbeat Detection Circuit*. Ph.D. thesis, Massachusetts Institute of Technology, Department of Electrical Engineering and Computer Science (2013).
69. Zhang, G., Shan, C., Kirenko, I., Long, X. & Aarts, R. M. Hybrid optical unobtrusive blood pressure measurements. *Sensors* **17**, 1541 (2017).
70. Nitzan, M., Khanokh, B. & Slovik, Y. The difference in pulse transit time to the toe and finger measured by photoplethysmography. *Physiol. Meas.* **23**, 85 (2001).
71. Tanaka, H., DeSouza, C. A. & Seals, D. R. Absence of age-related increase in central arterial stiffness in physically active women. *Arterioscler Thrombosis Vasc. Biol.* **18**, 127–132 (1998).
72. Cunha, R. S. et al. Association between high heart rate and high arterial rigidity in normotensive and hypertensive subjects. *J. Hypertens.* **15**, 1423–1430 (1997).
73. Siaron, K. B. et al. Blood pressure measurements are site dependent in a cohort of patients with neurological illness. *Sci. Rep.* **10**, 3382 (2020).
74. Payne, R. A., Symeonides, C. N., Webb, D. J. & Maxwell, S. R. J. Pulse transit time measured from the ECG: an unreliable marker of beat-to-beat blood pressure. *J. Appl. Physiol.* **100**, 136–141 (2006).
75. Ganti, V. et al. Enabling wearable pulse transit time-based blood pressure estimation for medically underserved areas and health equity: comprehensive evaluation study. *JMIR mHealth uHealth* **9**, e27466 (2021).
76. Badhwar, S. et al. Clinical validation of carotid-femoral pulse wave velocity measurement using a multi-beam laser vibrometer: the CARDIS study. *Hypertension* **81**, 1986–1995 (2024).
77. AtCor Medical Pty Ltd. SphygmoCor XCEL V1.3 Operator's Manual. AtCor Medical Pty Ltd, Sydney, Australia https://atcormedical.com/wp-content/uploads/simple-file-list/Downloads/SphygmoCor-XCEL-V1_3-Operators-Manual.pdf (2022).
78. Itamar Medical Ltd. EndoPAT 2000 Device User Manual. ManualsLib. https://www.manualslib.com/manual/1209421/Itamar-Medical-Endopat-2000.html#manual (2000).

79. Wang, R., Jia, W., Mao, Z.-H., Sclabassi, R. J. & Sun, M. Cuff-free blood pressure estimation using pulse transit time and heart rate. In *2014 12th International Conference on Signal Processing (ICSP)*, 115–118 (IEEE, 2014).
80. Gao, M. et al. Estimation of pulse transit time as a function of blood pressure using a nonlinear arterial tube-load model. *IEEE Trans. Biomed. Eng.* **64**, 1524–1534 (2016).
81. Zieff, G. et al. Acute psychological stress and pulse wave velocity: meta-analysis and recommendations for future research. *Psychophysiology* **62**, e70068 (2025).
82. Ma, Y. et al. Relation between blood pressure and pulse wave velocity for human arteries. *Proc. Natl. Acad. Sci. USA.* **115**, 11144–11149 (2018).
83. What is transmit power & transmit power control in wi-fi? https://thenetworkguys.wordpress.com/2022/11/10/what-is-transmit-power-transmit-power-control-in-wi-fi (2023).
84. detrend, https://www.mathworks.com/help/matlab/ref/detrend.html (2024).
85. Noise robust differentiators for second derivative estimation, http://www.holoborodko.com/pavel/downloads/NoiseRobustSecondDerivative. (2024).
86. Zhao, M., Adib, F. & Katabi, D. Emotion recognition using wireless signals. In *Communications of the ACM* (ACM, 2016).
87. Zhang, C.-B. et al. Delving deep into label smoothing. *IEEE Trans. Image Process.* **30**, 5984–5996 (2021).
88. Alastruey, J. et al. Arterial pulse wave modeling and analysis for vascular-age studies: a review from VascAgeNet. *Am. J. Physiol. Heart Circ. Physiol.* **325**, H1–H29 (2018).
89. Díaz, A., Galli, C., Tringler, M., Ramírez, A. & Cabrera Fischer, E. I. Reference values of pulse wave velocity in healthy people from an urban and rural Argentinean population. *Int. J. Hypertens.* **2014**, 653239 (2014).
90. Seeed Studio XIAO nRF52840 Sense - TinyML/TensorFlow Lite-IMU / Microphone - Bluetooth 5.0, https://www.seeedstudio.com/Seeed-XIAO-BLE-Sense-nRF52840-p-5253.html (2024).
91. PulseSensor, https://pulsesensor.com/products/pulse-sensor-amped (2024).
92. iNEMO inertial module: always-on 3D accelerometer and 3D gyroscope, https://files.seeedstudio.com/wiki/XIAO-BLE/ST_LSM6DS3TR_Datasheet.pdf (2024).
93. Dimora transparent film dressing, waterproof adhesive bandages 4 x 5 inch, https://dimoramedical.com/products/dimora-transparent-film-dressing-50-packs-waterproof-adhesive-clear-bandages-4-in-x-5-in (2024).
94. eBoot elastic spool, https://www.amazon.com/dp/B01DXRG7JO?ref=ppx_yo2ov_dt_b_fed_asin_title&th=1 (2024).
95. Adjustable fastening cable straps, https://www.amazon.com/dp/B09XMVVRH8?ref=ppx_yo2ov_dt_b_fed_asin_title&th=1 (2024).
96. Schulte, R. V., Prinsen, E. C., Schaake, L. & Buurke, J. H. Synchronization of wearable motion capture and EMG measurement systems. In *2022 International Conference on Rehabilitation Robotics (ICORR)*, 1–6 (ICORR, 2022).
97. Wu, C.-C., Chen, Y.-J., Hsu, C.-S., Wen, Y.-T. & Lee, Y.-J. Multiple inertial measurement unit combination and location for center of pressure prediction in gait. *Front. Bioeng. Biotechnol.* **8**, 566474 (2020).
98. Zhou, L. et al. How we found our imu: Guidelines to imu selection and a comparison of seven IMUs for pervasive healthcare applications. *Sensors* **20**, 4090 (2020).
99. Bannach, D., Amft, O. & Lukowicz, P. Automatic event-based synchronization of multimodal data streams from wearable and ambient sensors. In *European Conference on Smart Sensing and Context*, 135–148 (Springer, 2009).
100. Beutel, F., Van Hoof, C., Rottenberg, X., Reesink, K. & Hermeling, E. Pulse arrival time segmentation into cardiac and vascular intervals - implications for pulse wave velocity and blood pressure estimation. In*IEEE Transactions on Biomedical Engineering*, https://ieeexplore.ieee.org/document/9340235/?arnumber=9340235 (2021).
101. Gesche, H., Grosskurth, D., Küchler, G. & Patzak, A. Continuous blood pressure measurement by using the pulse transit time: comparison to a cuff-based method. *Eur. J. Appl. Physiol.* **112**, 309–315 (2012).
102. Wong, M. Y.-M., Poon, C. C.-Y. & Zhang, Y.-T. An evaluation of the cuffless blood pressure estimation based on pulse transit time technique: a half year study on normotensive subjects. *Cardiovasc. Eng.* **9**, 32–38 (2009).

Acknowledgements

We thank our participants at Carnegie Mellon University for their willingness to participate in our study. We thank Hongyang Li, Jason Li, Ran Bi, Veronica Muriga, Yifeng Wang, and Yiwen Song for their critical and important feedback on the manuscript. We thank Chengyi Shen and Rongbing Shen for designing the 3D printed enclosure for the mmWave radio. We thank Amit Thomas for assisting with the automated labeling of data from the contact-based reference sensors. We thank Tianyi Ren for assistance with the design of the contact-based reference sensors. We thank Jihang Jiang for the support on the subject recruitment process.

Author contributions

J.Z., K.Y., A.P., J.C. and S.K. conceptualized the study; J.Z. and K.Y. designed and performed the human subjects study, conducted the experiments, and performed the analysis under technical supervision by J.C. and S.K; J.Z., K.Y., A.P. and Y.L. developed the algorithms; G.W. designed the setup for the contact-based reference sensors; J.Z., K.Y. and J.C. wrote the manuscript; K.M. and S.K. edited the manuscript.

Funding

We acknowledge support from the NSF (2106921, 2030154, 2007786, 1942902, 2111751), ONR, AFRETEC, and CyLab-Enterprise to J.Z., K.Y., and S.K. We acknowledge support from the Center for Machine Learning and Health to J.Z., and the Massachusetts AI and Technology Center Pilot Award (5P30AG073107-05) to J.Z. and J.C. Any opinions, findings, and conclusions or recommendations expressed in this material are those of the author(s) and do not necessarily reflect the views of the above.

Competing interests

The authors declare the following competing interests: J.C. is a co-founder of Wavely Diagnostics, Inc. The remaining authors declare no competing interests.

Additional information

Supplementary information The online version contains supplementary material available at https://doi.org/10.1038/s41467-026-73453-x.

Correspondence and requests for materials should be addressed to Justin Chan or Swarun Kumar.

Peer review information : *Nature Communications* thanks anonymous reviewers for their contribution to the peer review of this work. A peer review file is available.